University of Rhode Island
DigitalCommons@URI

Open Access Master's Theses

2014

PREDICTION METHOD OF THE VORTEX INDUCED VIBRATION OF A ONE DEGREE-OF-FREEDOM SPRING-MASS SYSTEM.

Marina Iizuka Reilly-Collette
University of Rhode Island, marina.collette@gmail.com

Follow this and additional works at: https://digitalcommons.uri.edu/theses

Terms of Use
All rights reserved under copyright.

Recommended Citation
Reilly-Collette, Marina Iizuka, "PREDICTION METHOD OF THE VORTEX INDUCED VIBRATION OF A ONE DEGREE-OF-FREEDOM SPRING-MASS SYSTEM." (2014). *Open Access Master's Theses.* Paper 370.
https://digitalcommons.uri.edu/theses/370

This Thesis is brought to you by the University of Rhode Island. It has been accepted for inclusion in Open Access Master's Theses by an authorized administrator of DigitalCommons@URI. For more information, please contact digitalcommons-group@uri.edu. For permission to reuse copyrighted content, contact the author directly.

PREDICTION METHOD OF THE VORTEX INDUCED VIBRATION OF A ONE DEGREE-OF-FREEDOM SPRING-MASS SYSTEM.

BY

MARINA IIZUKA REILLY-COLLETTE

A THESIS SUBMITTED IN PARTIAL FULFILLMENT OF THE

REQUIREMENTS FOR THE DEGREE OF

MASTER OF SCIENCE

IN

OCEAN ENGINEERING

UNIVERSITY OF RHODE ISLAND

2014

MASTER OF SCIENCE THESIS

OF

MARINA IIZUKA REILLY-COLLETTE

APPROVED:

Thesis Committee:

Major Professor Jason M. Dahl

Stephen S. Licht

D.M.L. Meyer

Nasser H. Zawia

DEAN OF THE GRADUATE SCHOOL

UNIVERSITY OF RHODE ISLAND

2014

ABSTRACT

Vortex Induced Vibrations (VIV) are a critical problem in the offshore industry, where interaction between flexible immersed marine structures and natural currents result in large structural oscillations. These vibrations can result in fatigue life reductions, increased factors of safety, risk of unplanned failure, reduction in operational time, and may require costly mitigation strategies. Present methods of modeling VIV used largely in industry are limited to considering motion restricted to the transverse direction relative to flow. Semi-empirical prediction methods of VIV offer a good estimate for these vibrations, but expanding them to include inline body motion would create a prohibitive increase in the number of experiments required to properly characterise VIV, even at a single Reynolds number. This thesis documents the research, development, and implementation of a novel simulation method which combines VIV prediction with on demand experiments to significantly reduce the experimental effort.

Previous semi-empirical prediction methods use large databases of hydrodynamic force coefficients, obtained from forced motion experiments to predict VIV. The new method developed in this thesis conducts experiments on-demand, using the Newton-Raphson method to select new experiment conditions, in order to obtain a prediction using significantly fewer experiments. On-demand experimentation with autonomous test runs in a fully integrated experimental tank inform the simulation at each step in the iteration. The system is demonstrated to reproduce observed free vibration VIV data for cases of data varying by Reynolds number,and varying mass-damping parameters.

Results of the implementation of the system suggest a vast reduction in the time required to characterize VIV at unfamiliar Reynolds numbers, with the output verified in comparison to existing free vibration VIV data and prior forced motion

experiments done at limited Reynolds numbers. In doing so, the reduction in time and complexity makes possible the desired future objective of adding in-line oscillations to the prediction method, without the burden of an unwieldy number of forced motion experiments to perform.

ACKNOWLEDGMENTS

I would like to thank my advisor, Dr. Jason Dahl, for patiently teaching me scientific rigour and putting up with my stuffy formality, my wife Alexandria for her tireless support and occasional assistance with torquing chains and cutting aluminium, and my father for instilling in me a love of life-long learning without which this effort would not be possible. Due thanks must also be given to Amanda Perischetti for showing me the ropes at URI, and also to Fred Pease and Robin Freelander, whose machining work make this thesis possible. Likewise, my deepest appreciation is extended to the Narragansett Tribe of Indians. Their land, on which the University was built, and their own story of survival, were a stalwart and enduring reminder and example of why by each little step of effort the engineering profession has come from many false starts to try and make the world a better place.

DEDICATION

This thesis work is dedicated to the community of Oso, Washington, some of the early victims of the climate change this work in some small measure hopes to help mitigate, and also my childhood friends.

TABLE OF CONTENTS

ABSTRACT ii

ACKNOWLEDGMENTS iv

DEDICATION v

TABLE OF CONTENTS vi

List of Tables x

List of Figures xi

Chapter

1 Introduction 1

1.1 Motivation for Research 1

1.2 Chapter Overview 4

2 Background and Principles of VIV Simulation 6

2.1 Vortex Shedding 6

2.2 Vortex Induced Vibration 7

2.3 Nondimensional Parameters of VIV 9

2.3.1 General Nondimensional Parameters 9

2.4 Parameters affecting VIV 12

2.4.1 A review of select nondimensional parameters critical to VIV. 12

2.4.2 Prior VIV Research. 13

2.5 Introduction to VIV Simulation 18

2.5.1 Simulation with forced motion of a rigid cylinder 19

Page

2.5.2 Limitations of the Forced Motion Simulation 21

3 Methodology and Implementation 23

3.1 System Conceptualization 23

3.2 Algorithm Structure and Implementation 24

3.3 Physical System Components 26

3.4 System Control Components 30

3.5 System Functions 34

3.5.1 Central Control Function 34

3.5.2 Offset Correction function 35

3.5.3 PMAC Working Programme function 36

3.5.4 Download Program function 37

3.5.5 Gather Data function 38

3.5.6 Coefficient Finder 38

3.5.7 Selection Analyzer 43

4 Results and Analysis 46

4.1 Validation of experimental setup 47

4.2 Initial simulation attempts 49

4.2.1 Comparison with Smogeli. 50

4.2.2 Comparison with Vikestad. 50

4.3 Comparison with Khalak and Williamson. 52

4.4 Comparison with Gharib (1999). 57

4.5 Observations 61

5 Conclusions and Recommendations 66

Page

5.1 Principal Contributions of the Thesis 67

5.1.1 Development of the Algorithm. 67

5.1.2 Simulation of 1-degree of freedom results. 67

5.1.3 On Demand Simulation 68

5.1.4 Newton-Raphson Method 68

5.2 Future Recommendations 69

5.2.1 Sparse Database 69

5.2.2 2-degree of freedom implementation 69

5.2.3 Testing of VIV suppression devices 70

5.2.4 Continuous system simulations 70

5.2.5 Horizontal cylinder case 70

LIST OF REFERENCES 72

APPENDIX

A Force Coefficients and Charts used for Comparison 74

B Tabular Clv Data, Khalak and Williamson (1999) 78

C Tabular Clv Data, Gharib (1999) 79

D Derivations of the Nondimensional amplitude and frequency defining the 1-degree of freedom VIV case 80

D.1 Explanation of the Derivation 80

D.2 Variable Definitions 80

D.3 Derivation 81

D.3.1 Initial Derivation of m_a and b_a 81

D.3.2 Derivation for A* 83

Page

D.3.3 Derivation for f* 84

BIBLIOGRAPHY 86

List of Tables

Table		Page
1	Variables in the fluid	10
2	Variables in the fluid	11
3	List of Matlab Functions in Simulation System	31
4	Separate System Components	32
5	Options for the VIV Prediction Wrapper	36
6	Selected C_{Lv} test values at V_r= 6.76.	48

List of Figures

Figure **Page**

1 Results from Khalak and Williamson (Khalak and Williamson, 1999) showing the characteristic hysterisis in nondimensional amplitude response 15

2 Chart of C_{LV} as a function of A* and V_r as reproduced from Morse and Williamson (Morse and Williamson, 2009), at Re=12000 . . 17

3 A schematic of the spring-mass system for VIV, where m is mass, b is the coefficient of damping, k is the spring constant, and F fluid forcing function. 20

4 Flow chart for prediction algorithm 25

5 Image showing the experimental tank and carriage with a demonstration rig mounted. 27

6 A selected set of views of the experimental apparatus under construction. 27

7 The force sensor being tested during installation with its output shown on the screen behind. 29

8 SolidWorks models of the quick-change mount attached to the force transducer and the test piece interface mount for a 1.5-inch outer diameter VIV test cylinder. 30

9 Flow chart showing Matlab Functions 34

10 Actual position data, showing retrieved Gather Data 39

11 Green lines indicate change in position from the position and force datasets. Since these must be occurring at the same points in time, the two sets can have their positions (in iterations of data collection, i.e. sample points) correlated and normalized. . . . 41

12 Filtering Process, quality of signal improvement. 41

13 Raw force data from the six-axis force transducer as plotted upon its input to the Coefficient Finder. 42

Figure **Page**

14 C_L plotted in blue and inertia plotted in red as a function of time . 43

15 The results of an attempt to reproduce the Smogeli data, overlaid in red triangles from the original plot and re-projected to scale. 50

16 Vikestad actual data versus Vikestad reproduction. 51

17 Vikestad reproduction attempt modified by approximation from Govardhan and Williamson (Govardhan and Williamson, 2006). . . 52

18 Vikestad normalized to Re = 16500 overlaid across Williamson forced motion plot for C_{lv} 53

19 Reproduction points plotted over Khalak and Williamson (Khalak and Williamson, 1999) original chart. 54

20 Convergence data for Khalak and Williamson reproduction, with Khalak and Williamson (Khalak and Williamson, 1999), from guessed A* and Vr values for each U* cut point. 56

21 A* vs. V_r for the case of Gharib (Gharib, 1999) and the reproduction of Gharib's data using the forced motion simulation system. 59

22 Plot of Convergence for Simulation of Gharib (Gharib, 1999) 60

23 Iterations to Convergence for Khalak and Williamson (Khalak and Williamson, 1999) reproduction 63

24 Iterations to Convergence for Gharib (Gharib, 1999) reproduction . 65

CHAPTER 1

Introduction

Vortex Induced Vibrations (VIV) are self-limiting dynamic fluid-structure interactions caused by forces due to vortex shedding. They are a canonical problem in fluid dynamics, and experience broad applicability in engineering to the omnipresence of bluff bodies in engineering applications. When an object undergoes VIV, it experiences vortex shedding as a result of flow across its bluff body profile. If the shedding frequency approaches the natural frequency of the object, large amplitude motions occur (Williamson and Govardhan, 2004) (Dahl, 2008). Structures from mooring cables to spar buoys experience these resulting large amplitude motions can impact their fatigue life and the general operation of these structures.

1.1 Motivation for Research

VIV is a critical problem in industry (Williamson and Govardhan, 2004) for the design of immersed structures. Offshore structures of the type which can experience VIV include mooring cables, towed arrays, and drilling and production risers. Due to their extreme length, they act similar to a string or tensioned beam. These objects are typically bluff bodies in the direction of current flow, usually cylinders, and flexible due to their length. These structures typically exhibit a wide range of natural frequencies and structural mode shapes, and simultaneously encounter complex sheared and directional currents.

Since VIV consist of interactions between a structure and surrounding fluid, large-scale simulation of the phenomenon is extremely difficult. Many simplifying assumptions must be made to produce models of VIV for predictive purposes. An initial assumption is that the long, flexible structure may be modeled as a flexibly mounted solid structure. This is acceptable if the assumption is made that the

solid structure is a small element of the long flexible structure. In this case, essentially treating the solid structure as a finite element of the long flexible structure, reduction of the motion to a spring mass system is possible. Additional typical assumptions for this case include assuming the body motion and forcing functions are sinusoidal, assuming motion is restricted to be perpendicular to the flow direction (hence called 'transverse'), and assuming the forcing function is a single frequency. These assumptions may lead to order of magnitude inaccuracies in fatigue life estimation from incorrect estimate of fatigue loading (Modarres-Sadeghi et al., 2010). Traditionally these inaccuracies are compensated for by conservative design practices such as large factors of safety, but with expansion of the offshore industry into new deepwater projects such as offshore wind farms, ocean thermal energy converters (OTEC), and wave/tidal energy mooring systems, conservative engineering practices prohibit cost-effective design. Within the limits of the motion described with these simplifying assumptions, several excellent reviews are available (Sarpkaya, 2004), (Williamson and Govardhan, 2004), (Bearman, 1984).

The classic simplification for only transverse motion is normally referred to as a 1-degree of freedom motion. VIV in the natural environment results in both transverse *and* in-line motions, collectively causing a sort of figure eight shape to the bod motion. Thus a more accurate representation of the phenomenon would allow for movement along the in-line (with the fluid velocity field) axis as well (Jauvtis and Williamson, 2004), (Dahl, 2008). Naturally, the successful simulation of VIV with 2-degrees of freedom would be desirable to improve the VIV prediction by accounting for forces more representative of those experienced by long, flexible bodies.

Simulations of VIV through forced motion has been shown to reproduce VIV for a 1-degree of freedom spring-mass system (Morse and Williamson, 2009), but

these simulations are only valid at the Reynolds number for which experiments were performed. Using traditional semi-empirical modelling methods for response prediction based on a force coefficient database, it is impossible to perform the number of experiments necessary to fully describe 2-degree of freedom VIV.

The objective of this research is to obtain a new algorithm for prediction of motion in 1-degree of freedom VIV that is applicable across any Reynolds numbers for which experiments can be performed. Instead of using a Navier-Stokes solver combined with a structural model, this method implements experiments to determine the fluid forces that are then used in balancing the equation of motion describing the system. The method to be developed is inherently general, allowing for simulation at varying Reynolds numbers. Expansion to larger degrees of freedom governing the motion of the body is anticipated in future work, but is not covered within the scope of this thesis. The outcome of this proposal will be a functional experimental system and methodology which will make future 2-degree of freedom VIV modelling possible. This will be demonstrated by showing the algorithm works for modelling the response of a 1-degree of freedom system.

The research undertaken for this thesis entailed development of a general algorithm for combining on-demand experiments with the solution of the body equations of motion to predict VIV for the case of a rigid cylinder segment. In doing so, the proposed method achieves substantial reductions in the time and experimental runs required for predicting one degree of freedom VIV motions. This method requires between one and twenty experiments to achieve the prediction, in comparison with Gopalkrishnan (Gopalkrishnan, 1993), requiring 306 exerpiemnts for a sparse database and Morse and Williamson (Morse and Williamson, 2009), requiring 5,680 for a dense database.

It is important to note that the objective of this thesis was to develop and

implement the algorithm. The data which was gathered has been observed before and acts as a validation to the algorithm. This thesis therefore details the design, construction, systems architecture, and programming of the 1-degree of freedom forced motion research assembly, and includes validation of its ability to produce correct results corresponding to a range of different inputs (Reynolds number, nondimensional mass parameter) for various free vibration experiments which have previously been conducted.

1.2 Chapter Overview

Chapter 2 provides background information on the phenomenon of VIV. It reviews the literature that was used in this research and thesis, explains the fundamental requirements of VIV simulation, and explains the specific nature of VIV. Included in the review is the dimensional analysis of the fundamental parameters of the VIV phenomenon and of the simulation of VIV, and an explanation of the critical nature of the nondimensional parameters governing VIV. This chapter provides detail on thegeneral phenomenon of vortex shedding. A brief overview of the relevance of the developed algorithm and system setup to further 2-degree of freedom research will also be provided.

In Chapter 3, the methodology of the experimental system is explained in detail. It describes the systems architecture and implementation of the simulation method. The integration of the motion control, data acquisition and prediction are explained. This chapter also explains the data processing techniques used in this thesis. As the algorithm itself was the objective of the research, it is appropriate to detail how the system was constructed to realise and test the algorithm. This chapter will therefore detail the construction of the whole test apparatus, and the synchronization of its components. The nature and construction of the physical elements, mechatronic elements, and computational elements will be detailed and

the integration of these elements as well. Challenges which were overcome to realise successful operation of the system will be covered and explained.

For Chapter 4, validation of the system for purposes of simulating free vibration experiments in VIV will be shown. These results demonstrate that the system works correctly and successfully reproduces free vibration experiments. In free vibration experiments, the phenomenon of VIV is directly observed, hence reproducing such experiments *is by definition* the successful simulation of VIV. Therefore, Chapter 4 discusses the simulation of free vibration experiments, the functioning of the system, and the limitations of the system as discovered through conduct of various simulations. Comparisons are made to a variety of datasets with a range of Reynolds numbers and physical parameters governing the phenomenon of VIV.

Finally, Chapter 5 contains conclusions and recommendations for future research. These include a discussion of the results of system operation covered in Chapter 4, as well as their implications for VIV research. The success of the system in the context of future applicable to 2-Degree of Freedom systems in the future is also discussed. Contributions to science by this thesis are clearly outlined based on the results of this system implementation.

CHAPTER 2

Background and Principles of VIV Simulation

2.1 Vortex Shedding

At its most fundamental, vortex shedding occurs behind a bluff body in a current. At extremely low Reynolds numbers, vortices do not form, or form and do not separate. At Reynolds numbers above Re = 40, vortex *shedding* begins to occur, driven by small perturbations in the flow or on the surface of the body (Blevins, cited in (Dahl, 2008)). This alternating shedding of vortices is referred to as the "Karman Vortex Street", originally described by Von Karman in 1912 (cited in (Gopalkrishnan, 1993)). A negative pressure gradient upstream of the body forces fluid to adhere to it; on the back of the body, the pressure gradient switches signs and causes shear, which leads to separation and vortex shedding. The frequency of shedding is dependent on flow speed and size of the object, and is governed by the Strouhal number, defined as:

$$St = \frac{f_s d}{U} \tag{1}$$

The Strouhal number represents a constant of proportionality–for subcritical Reynolds numbers–in the relationship of the cylinder diameter and the velocity of the free stream with the frequency of vortex shedding (Gopalkrishnan, 1993). It is generally held to be approximately St = 0.2 in all cases of interest, though Bearman (Bearman, 1984) observed in the critical regime (Re > 2x10^5) Strouhal numbers up to St = 0.46. Vortex shedding continues not merely at Reynolds numbers immediately above Re = 40, but also well into the critical range, though it is not always the classic regular shedding of the Karman Vortex Street, but may also be irregular (Bearman, 1969); however, for most cases of interest regular

vortex shedding is the dominant feature (Bearman, 1984). This research focuses on the subcritical regime and generally on behaviour observed between $1x10^3 < Re < 5x10^4$. Here, vortex shedding can be well understood to be heavily influenced by the Reynolds number, but also parameters such as surface roughness and free stream turbulence may influence the phenomenon (Bearman, 2011).

Though in general this problem is not at all limited to cylinders, the commonality of cylinders in engineering applications makes them the primary focus of research into the phenomenon. In the case of VIV, vortex shedding remains similar to that behind a stationary cylinder in flow, but interactions with the motion of the body can cause considerable differences to the case of a fixed body (Bearman, 1984). For purposes of VIV research, the variability of vortex separation mentioned is particularly interesting. Vortex shedding on a fixed body occurs according to the classic Karman street mode. In an oscillating body, however, additional modes may occur (Williamson and Govardhan, 2004).

2.2 Vortex Induced Vibration

A principle difference between simple vortex shedding and Vortex Induced Vibration is the freedom of the bluff body experiencing vortex shedding to freely move, in at least one degree of freedom. As flow speed is increased, a condition is reached where the frequency of vortex shedding f_s becomes sufficiently close to the natural frequency of the body f_n so that pressures from the vortices being shed in a non-regular fashion begin to drive motion. In short, when vortex shedding occurs at a frequency close to the natural frequency of an elastically mounted or flexible cylinder, large amplitude motions may occur. When the motion is constrained to only move perpendicular to the direction of the current (transverse motion), these motions may be up to 1.5 - 2.0 times the diameter of the body (Bearman, 1984). Additional in-line directional motion will also occur if the body is free to move

in-line with the direction of the current (Williamson and Govardhan, 2004).

It is important to observe that VIV occurs for many object shapes. Though this research limits itself to cylinders due to their universality in most common applications (Bearman, 1984), any bluff body in flow can in principle experience VIV. Furthermore, for the case of cylinders–typically in industrial settings–they most usually experience VIV from being long and flexible. Cylinders used in VIV research, however, are often rigid cylinders that are elastically mounted at both ends in order to simplify the problem when studying the basic physics of the fluid-structure interaction.

Vortex induced vibration does not have vortex shedding patterns limited to the classic Karman street case. The complex interaction of body motion and vortex shedding may produce a series of wake patterns, and the condition of lock-in, where the cylinder's oscillation frequency and the vortex shedding frequency match. In addition to the classic Karman street mode, called the 2S mode and featuring two single vortices per cycle, there may also be a 2P with two vortex pairs per motion. This means that VIV sees a feedback loop between both vortex motion and body motion (Williamson and Govardhan, 2004). The different vortex wake modes affect the phasing of the force exerted on the cylinder.

Lock-in occurs when the fluid-structure dynamic reaches a final equilibrium through the matching of effective impedances between the fluid and structure. The mechanism stabilizes when the frequency of vortex shedding and natural frequency are similar. The forces caused by vortex shedding can change the effective mass of the system and force the system to be excited at an effective natural frequency, the lock-in frequency. As a result, lock-in resonance is possible over a much wider range than is typical in mechanical systems (Dahl, 2008).

When a body experiencing vortex shedding is free to oscillate, it may do

so with relatively large amplitude motions in more than just the transverse direction. As Bearman reviews, for a very long time, it was assumed that motion could be simplified to the 1-dimensional case (i.e., purely transverse motion) (Bearman, 1984). This has been acceptable for scientifically studying the phenomenon of VIV, but in engineering practice, observed vibrations are much more complex, including not just in-line motion but even 3-dimensional vibrations of slender structures. Furthermore, the in-line motion mentioned by Williamson and Govardhan (Williamson and Govardhan, 2004) can reach 25% of the maximum typical transverse motion (Dahl, 2008). This has been shown to have a substantial impact on fatigue life through dramatically different hydrodynamic forcing, making a more complete modeling effort of 2-degree of freedom VIV critical to accurately predicting VIV and its impacts. The 1-degree of freedom case has been amply studied, as briefly overviewed above. Though the system developed in this thesis is for a 1-degree of freedom simulation, its purpose is to provide a proof of concept that can be extended to higher dimensional systems.

2.3 Nondimensional Parameters of VIV

Both the nondimensional parameters required in solving for the motion of the body and those used to characterise the force on the body shall be covered.

2.3.1 General Nondimensional Parameters

General parameters are those applicable to the phenomenon of VIV in general, as opposed to strictly the case of the forced motion simulation. The first table comprises a list of variables, showing the symbol for the variable, its description, units, base form in Buckingham PI theorem, and type. The type references whether, in the typical case of VIV, the variable is controllable, fixed, or a value which is genuinely variable rather than at the discretion of the experimenter. Likewise these

are the values strictly for the fluid force. Influence of the components of the cylinder being analysed are handled separately. A certain number of nondimensional parameters are required to correctly define the problem.

Symbol	Parameter Description	Units	Base Form	Type
f	Frequency of oscillation	1/s	1/T	Variable
f_n	Natural frequency of the cylinder	1/s	1/T	Fixed
m	Mass of the cylinder and any associated apparatus	kg	M	Fixed
k	Spring constant of the system	kg/s^2	M/T^2	Fixed
b	System damping	kg/s	M/T	Fixed
D	Diameter of the cylinder	m	M	Controlled Variable
L	Immersed length of the cylinder	m	M	Controlled Variable
f_s	Frequency of vortex shedding	1/s	1/T	Dependent Variable
A	Amplitude of body motion (transverse)	m	L	Controlled Variable
ρ	Density of water	kg/m^3	M/L^3	Controlled Variable
μ	Viscosity of water	kg/(s*m)	M/(T*L)	Controlled Variable
U	Free stream velocity	m/s	L/T	Controlled Variable
F	Transverse fluid force	$kg*m/s^2$	$M*L/T^2$	Variable

Table 1: Variables in the fluid

Not all are strictly required, for example, the f* parameter stems from the fact that f* may also be defined as $f^* = \frac{V_r}{V_{rn}}$, such that it is not an independent non-dimensional parameter as it can be constructed from V_r and V_{rn}, but is universally used and very convenient, thus included. There are several names for many of these parameters used in literature for each variable as noted. Finally, the following dependent nondimensional parameters are of particular interest in successfully deriving actual amplitude and frequency of motion from recorded force data during the experiment process; their derivations are provided in Appendix D.

Non-dimensional group	Parameter Description	Units
V_{rn}	Nominal Reduced Velocity	$U/(f_n D)$
V_r	Reduced Velocity	$U/(f D)$
A*	Nondimensional Amplitude	A/D
St	Strouhal Number	$(F_s D)/U$
f*	Frequency ratio (nondimensional frequency)	f/f_n
ζ	Damping ratio	$\frac{b}{2\sqrt{k*m}}$
U*	Nominal Reduced Velocity / Nondimensional velocity	$\frac{U}{f_n D}$
λ^* (V_r)	Nondimensional wavelength/Reduced Velocity	$\frac{U}{fD}$
C_L	Coefficient of Lift	$\frac{F}{0.5\rho U^2 DL}$
Re	Reynolds Number	$\frac{\rho U D}{\mu}$
m*	Mass ratio (nondimensional mass)	$\frac{4m}{\pi\rho D^2 L}$

Table 2: Variables in the fluid

$$C_L = \frac{F}{0.5\rho U^2 DL} \tag{2}$$

$$C_{La} = C_L cos(\phi) \tag{3}$$

$$C_{Lv} = C_L sin(\phi) \tag{4}$$

$$C_m = \frac{1}{2\pi^3}\frac{C_L cos(\phi)}{A*}(\frac{U*}{f*})^2 \tag{5}$$

These equations represent the lift force magnitude nondimensionalized, and the respective components of the lift coefficient thus defined. The Coefficient of lift in phase with acceleration C_{La} and the coefficient of lift in phase with velocity C_{Lv} characterise the added mass and added damping respective as described in equation 12. Look-up tables of these coefficients comprise the classic large database which

can be used to solve the single degree of freedom spring-mass-dashpot system equation in time.

These nondimensional parameters are then used to normalize equation 12, giving equations 6 and 7 as per Khalak and Williamson (1999). These equations govern the motion of the body based on the force input and are used in this thesis to determine the solution of the body motion.

$$A* = \frac{1}{2\pi^3}\frac{C_L cos(\phi)}{C_m}(\frac{U*}{f*})^2 \tag{6}$$

$$f* = \sqrt{\frac{m* + C_m}{m*}} \tag{7}$$

2.4 Parameters affecting VIV

2.4.1 A review of select nondimensional parameters critical to VIV.

Tables 1 and 2 list the nondimensional parameters and how they relate to the problem variables. The reduced velocity V_r serves as a comparison of the free-stream velocity with respect to the transverse velocity of the cylinder. Many of the other nondimensional parameters may have multiple values for a single value of V_r, depending on the fluid-structure interaction, so that multiple stable motions are possible at a given V_r. This has led to the use of U*, the nondimensional velocity (based on f_n rather than f) to plot nondimensional amplitude responses, but this is undesirable as it can mask important information in VIV behaviour when plotted (Khalak and Williamson, 1999).

The Coefficient of Added Mass, Coefficient of Lift, Nondimensional Amplitude, and Nondimensional Frequency are functions V_r; they normalize the cylinder motion and the forces exerted upon it, and are thus relatively straightforward. The mass ratio, however, is a measure of the relative size of structural mass and the

mass *displaced* by the structure. In air the mass ratio is extremely large; in water it is small, such that ocean structures typically have an $m^* = 3.0$. ζ, the damping ratio, is structural damping in respect to critical damping. It would be expected that $\zeta = 0.05$ for a typical marine structure. An extremely common parameter in VIV research is $m^*\zeta$, the mass-damping parameter. It is generally accepted that this parameter directly affects the amplitude response for the cylinder, and that as it decreases, the cylinder will oscillate with larger amplitudes (Dahl, 2008), (Govardhan and Williamson, 2006).

Reynolds number is based on cylinder diameter in addition to the requisite flow velocity. Multiple studies (Morse and Williamson, 2009),(Govardhan and Williamson, 2006) have shown a strong correlation between Reynolds number and the amplitude response and forces of VIV, the correlation being positive. Due to the wide range of Reynolds numbers at which structures may experience VIV, it must be noted that this correlation is one of the factors driving a need for more research on Reynolds number effects in VIV.

2.4.2 Prior VIV Research.

Khalak and Williamson (Khalak and Williamson, 1999) performed a series of experiments at very low values of the mass-damping parameter. Khalak and Williamson used a vertically mounted cylinder allowed to oscillate in a flow channel in the transverse direction. Reynolds number was held relatively constant. These experiments, very well documented, were the first to observe the "collapse" of the data when U^* was normalized by f^*, showing that $f = f_n$ is not always a reliable assumption to be made in VIV. (Khalak and Williamson, 1999) reported results arguing for the $m^*\zeta$ mass-damping parameter being critical in influencing response. This means that the *maximum* response is a function of the system mass and damp-

ing. They also argued that its value further determined whether or not a hysteriesis in the response would occur, though this is debated (Sarpkaya, 2004). For large mass ratios the cylinder oscillation frequency will be close to the vortex shedding frequency *and* the natural frequency of the body, but over a larger range of mass and damping values this is not necessarily the case (Khalak and Williamson, 1999). The Reynolds number clearly also plays some role in the response amplitude, and Sarpkaya (Sarpkaya, 2004) has assessed that Khalak and Williamson have underestimated its role in determining the hysteriesis.

The aforementioned hysteriesis where the amplitude at the stable VIV case may jump between two different values over an extremely small range of nondimensional velocity (U*) has been well demonstrated, even if its cause has not been and is still debated. It is not always present, and indeed in the results presented in this thesis did not occur at very high m*ζ values, but not enough variation in m*ζ for the simulations conducted in this thesis research were conducted to comment further on this matter. It remains that the hysteriesis is a particular point of interest in continuing VIV research. In fact, per (Morse and Williamson, 2009), this effect can occur over exactly the same U* value, leading to a series of characteristic branches of maximum amplitudes as shown in Fig.1.

Govardhan and Williamson (Govardhan and Williamson, 2006) report the collapse of data in the classic 'Griffin' plot if Reynolds number is taken into account as an extra parameter. Govardhan and Williamson illustrate the strong dependence of lift forces in VIV on Reynolds Number, as does the work of Morse and Williamson from (Morse and Williamson, 2008). Williamson and Govardhan (Williamson and Govardhan, 2004) provides a review of VIV. It also provides a summary of characterized wake vortex modes.

Smogeli, et al (Smogeli et al., 2003) developed a force feedback system for

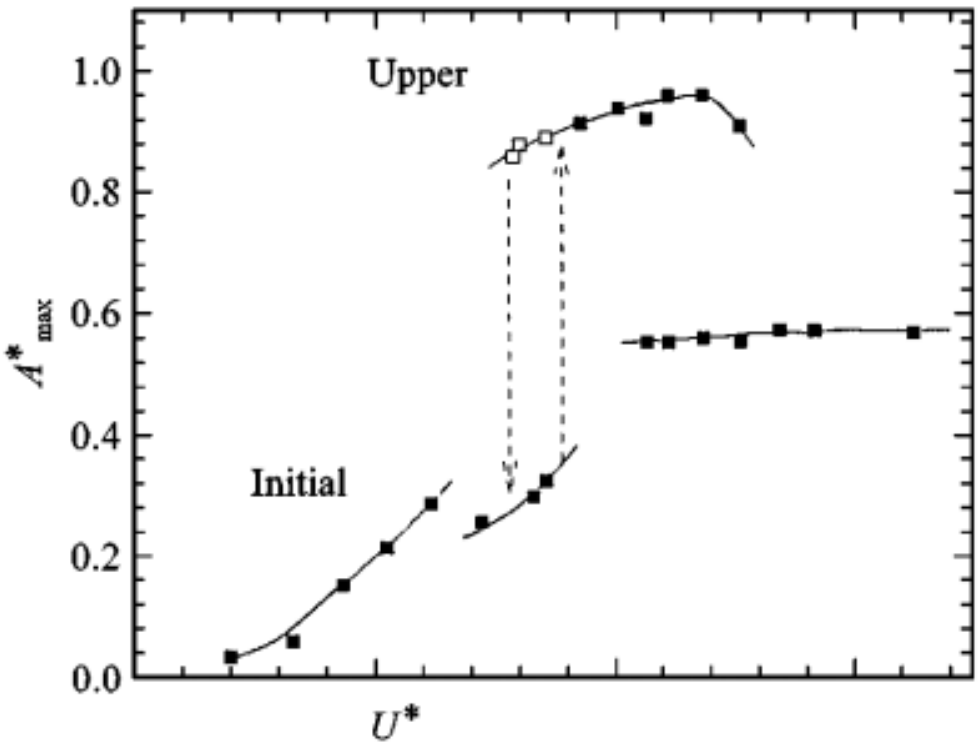

Figure 1: Results from Khalak and Williamson (Khalak and Williamson, 1999) showing the characteristic hysterisis in nondimensional amplitude response

simulating VIV. VIV could be modeled using a force feedback system where force coefficients were calculated in real time, with the system responding to forces in real time.

Vikestad (Vikestad et al., 1997) reported primarily on results of a combination of VIV and a structural vibration input to the system (representing a hypothetical mechanical vibration to complement that being delivered by the fluid-structure interaction). They provided some initial control data for free vibration cases as well. Both the data from Smogeli and Vikestad were gathered via a horizontally suspended cylinder and the Reynolds number allowed to vary between any particular point of U* and A* in a data-set, unlike that of Khalak and Williamson (Khalak and Williamson, 1999).

Gharib (Gharib, 1999) conducted a series of free vibration experiments across low ζ values and a wide range of m* values. Gharib, like Khalak and Williamson, used a vertically mounted cylinder and held Reynolds number constant.

Morse and Williamson (Morse and Williamson, 2009) reported on results showing that forced-motion experiments could perfectly VIV, through the methods described earlier. The forced motion experiments performed by Morse and Williamson (Morse and Williamson, 2009) provide a high resolution measurement of C_{LV} and C_m as functions of A* and V_r. Fig.2 shows a sample contour plot of C_{LV} from Morse and Williamson.

The 5680 experiments performed to produce Fig.2 represent a parameter resolution of 70, where A* and V_r were varied with 70 different values, allowing for extremely fine resolution of the experiments. Not all of these experiments are performed in a region where free vibration VIV will occur, hence not all of these experiments are necessary if one wants to use them to predict VIV. This highlights the necessity for a different approach to solving this problem if extended to

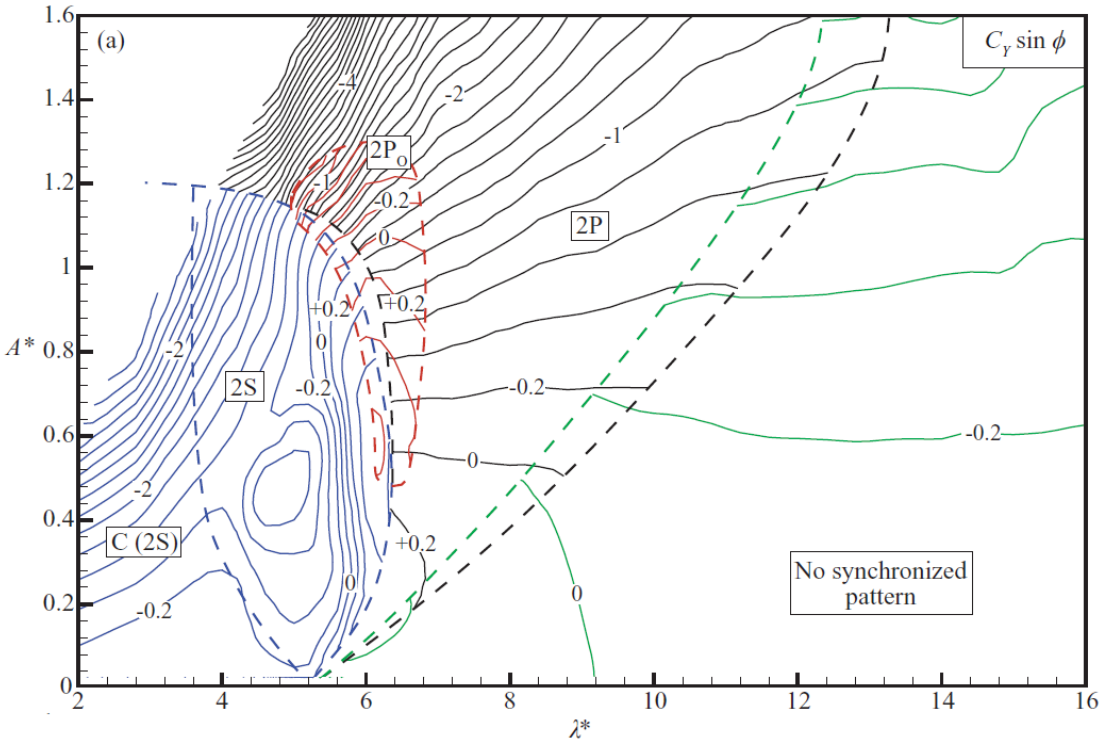

Figure 2: Chart of C_{LV} as a function of A* and V_r as reproduced from Morse and Williamson (Morse and Williamson, 2009), at Re=12000

2-degree of freedom systems.

For 2-degree of freedom systems the number of parameters governing the body motion increases from 2 to 4 (not including Reynolds number), thus the parameter resolution must be increased to the fourth power, yielding approximately 24,000,000 experiments if the relative accuracy of the system used by Morse and Williamson is maintained. Nonetheless, the Morse and Williamson experiments served to *validate* the method of using forced rigid cylinder motions to simulate VIV perfectly. It is not, strictly speaking, necessary for that parameter resolution to be used in all VIV research. Their effort was simply required to demonstrate that the forced motion method was indeed *accurate.* Only a single experiment, with a single V_r and a single A*, is actually necessary to obtain the correct solution for VIV–if we knew where it was, which we do not, thus requiring a very large number of experiments, with sufficient parameter resolution to verify that those experiments were correct; only then a mathematical simulation of VIV could be solved using these data.

2.5 Introduction to VIV Simulation

Methods used for VIV simulation are varied, but may be essentially characterised into two branches. These branches comprise direct numerical simulation, such as a full Navier-Stokes solver, and semi-empirical methods. Present semi-empirical methods include developing a large database of force coefficients by running experiments and then solving for the motion of the body. Examples of forced motion databases include Gopalkrishnan (Gopalkrishnan, 1993) and Morse and Williamson (Morse and Williamson, 2009), additional examples are cited in Hover, et. al. (Hover and Triantafyllou, 1998). Semi-empirical codes used in industry for predicting the motion of long slender structures include SHEAR7, VIVA, (Mukundan and Triantafyllou, 2010) and VIVANA (Chaplin et al., 2005)

All of these programmes use some form of experimentally derived force coefficients to predict VIV, however each code is limited in its ability to incorporate high degrees of body motion without the need for additional force information from experiments.

One problem with all of these programmes is the need to generate a massive force coefficient database before solving for the body motion. This is typically accomplished through forced motion experiments. For predicting VIV with these programmes a slender body representing the structure is first assumed. It is presumed that slender body theory is valid, such that the fluid force can be represented by the equivalent two dimensional force at any particular cross section of the three dimensional body. The force on a cross-section of the body can then be represented as that of a single rigid cylinder undergoing a particular motion. An additional simplification assumes 1-degree of freedom motion for the cylinder, such that the body only moves perpendicular to the current. This is justified on the grounds that most observed motion from VIV occurs in the transverse direction. With the number of simplifications thus proposed, it then becomes possible to establish the database of hydrodynamic coefficients by varying two parameters, here called A^* and V_r. Forced motion experiments may then be performed, varying A^* and V_r to measure the desired forces.

2.5.1 Simulation with forced motion of a rigid cylinder

The forcing function for the body's motion is determined by conducting an experiment of forced sinusoidal motion of a rigid cylinder through a free stream, measuring the forces exerted on the body. This allows creation of the database for a variety of amplitudes and frequencies which can then be used to solve for VIV of a cylinder with given structural properties. The simplest form of this solution method comes from considering a one degree of freedom spring mass system. The

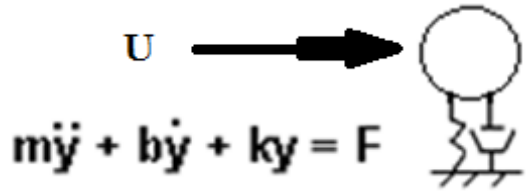

Figure 3: A schematic of the spring-mass system for VIV, where m is mass, b is the coefficient of damping, k is the spring constant, and F fluid forcing function.

equation is given as per Fig. 3.

We can assume phase-shifted harmonic forcing and harmonic motion, based on observations of 1-degree of freedom systems undergoing VIV. This allows for the expansion of the forcing term, F:

$$y = Asin(\omega t) \tag{8}$$

$$F = Lsin(\omega t + \varphi) \tag{9}$$

$$F = Lcos(\varphi)sin(\omega wt) + Lsin(\varphi)cos(\omega t) \tag{10}$$

This result is composed of two terms, one in phase with acceleration and one in phase with velocity respectively. If we assume the force in phase with acceleration behaves as an added mass m_a and the force in phase with velocity behaves as an added damping b_a, then we have:

$$F = -m_a y" - b_a y' \tag{11}$$

$$(m + m_a)y" + (b + b_a)y' + ky = 0 \tag{12}$$

If the magnitude of the forces are known as a function of frequency and amplitude the equations may then be solved iteratively to find the amplitude and frequency of vibration, the forces, of course, being derived from the force motion experiment described above, and m_a and b_a become:

$$m_a = \frac{C_m \rho \pi d^2 l}{4} \tag{13}$$

$$b_a = \frac{C_{Lv} \rho d U^2 l}{2A * \sqrt{\frac{k}{m+m_a}}} \tag{14}$$

As opposed to a typical forced single degree of freedom system, the form of the hydrodynamic force, F, is such that the equation can be written as a free vibration with modified mass and damping. There are other differences, furthermore. The most important of these, which must be carefully observed, is that m_a and b_a are *functions of the amplitude and frequency of oscillation. Thus*, the problem is nonlinear, even if it can be represented as a linear equation for a single set of values of m_a and b_a, it cannot actually be solved as a simple linear equation. It is for this reason that experimentation to build up a large database of force coefficients is the present standard practice in forced motion simulation for VIV. The equation of motion must therefore be solved iteratively since m_a and b_a will change as a function of the motion. The force database provides a simple way to transition between values of m_a and b_a for given cylinder motions.

2.5.2 Limitations of the Forced Motion Simulation

As the added mass and damping are functions of the amplitude and frequency of oscillation, it is thus necessary to solve this equation interatively. Rather than being able to analytically solve for the solution of the equation, at each change in amplitude/frequency in the solution of the equation there must be input from data derived from experimentation.

Per Morse and Williamson (Morse and Williamson, 2009), a given database is furthermore only applicable at the Reynolds number for which it was gathered. Morse and Williamson (Morse and Williamson, 2009) predicted the for the perfect

prediction of Vortex Induced Vibration of a 1 degree of freedom spring mass system at a single Reynolds number with equivalent mathematical conditions in the simulation as to the desired real-world or free vibration experimental case, however they showed that there can be significant differences in observed fluid forces, even for moderately different Reynolds numbers.

CHAPTER 3

Methodology and Implementation

The developed algorithm which forms the thesis objective and the constructed experimental apparatus to achieve this objective are descibed in the following chapter.

3.1 System Conceptualization

The system consists of the algorithm, administered through a control program and the physical plant. Collectively the program and the physical plant implement the algorithm. The program itself consists of a series of sub-programs. Each of the sub-programs performs a specific function. Programs were written to establish communication between components of the physical plant, that processed these resultant data, performed calculations with these data, and finally used data to make predictions. Likewise the physical plant components were physically wired and integrated for commands to be executed and data recorded.

In this system, the algorithm implements a semi-empirical simulation, the general concept of which is described in Chapter 2, and which herein is an adaptive and predictive algorithm. The predictive algorithm uses an iterative process to determine new experiments to supplement the solution of the body equation of motion, rather than performing a pre-defined experimental set *a priori*.

The development of the semi-empirical simulation algorithm detailed herein takes advantage of a forced motion that mimics VIV while force coefficients are recorded from the measured force output of this motion, being no different in that respect than the process described in Chapter 2.3. The difference is that in traditional methods C_{Lv} and C_m are determined *a priori* by conducting a large series of experiments varying A^* and V_r to produce a database of fluid force coeffi-

cients. The solution may then be obtained iteratively by integrating the equation of motion over one half cycle and updating the fluid force based on the current motion parameters, or by converging on the C_{LV} value corresponding to the appropriate structural damping. In the system developed here, experiments are only performed as necessary to determine whether a solution has been obtained. In order to achieve this for the equation of motion (equation 2), one must determine a balance between the fluid force and the structural forces. In the case of VIV, we know that the amplitude of motion is limited by fluid damping. A steady limit cycle is reached when the fluid force in phase with velocity perfectly cancels the structural damping forces, leading to an effective resonant situation (the only remaining forces are the cylinder inertia, added mass, and spring restoring force).

The equations of motion and forcing functions are non-dimensionalized for generality. As the solution is then nondimensional it is fully scalable as long as all nondimensional parameters are matched. This is not trivial, however, as the fluid force terms C_{Lv} and C_m are known to be functions of Reynolds number (Morse and Williamson, 2009).

3.2 Algorithm Structure and Implementation

A flow chart of the developed algorithm is shown in Fig. 4

Requirements for the successful implementation of this algorithm included the automated communications between the algorithm and its controlling script, the PMC that directly controls the motors, and the force sensors which provide input to cue the next experiment. Using a search heuristic algorithm that can select new amplitude and frequency values for an on-demand experiment based on analysis of the force and position data from the prior experiment, the process takes data from the prior experimental run, analyzes it, and based on these data selects the new values for the next experiment.

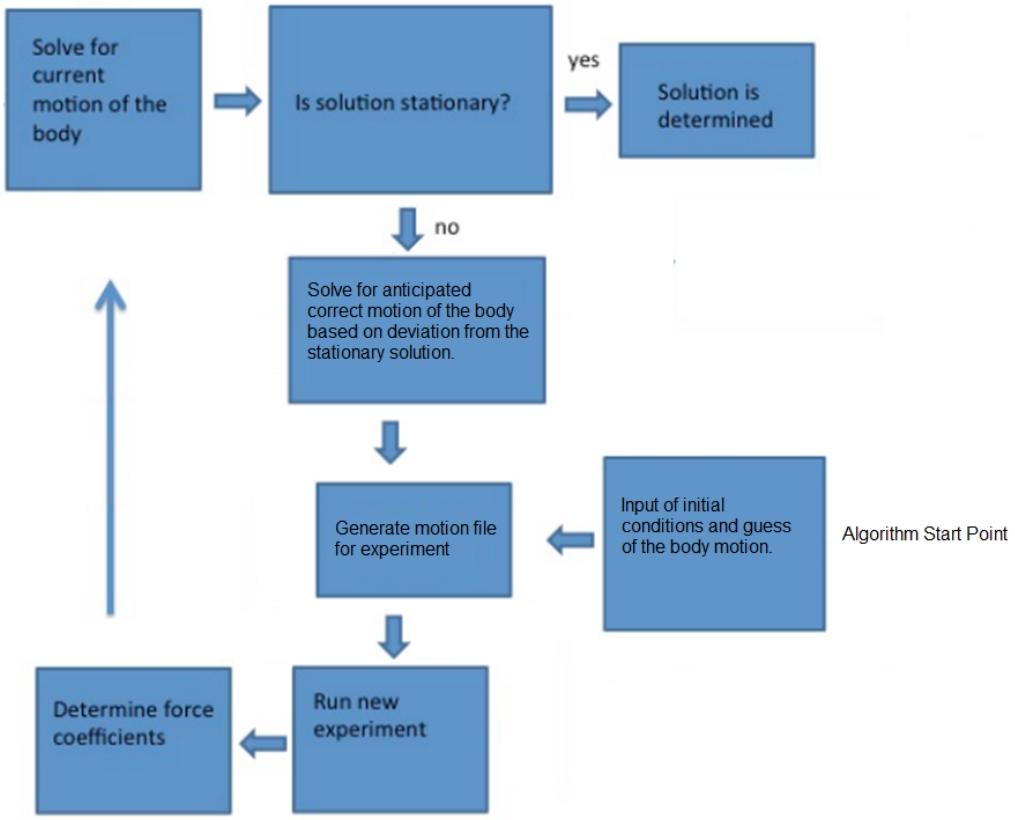

Figure 4: Flow chart for prediction algorithm

Matlab was used as the integration mechanism of the system components. A series of matlab functions were written to integrate the system components–both the physical plant and the sub-functions required for executing specific tasks in the algorithm–into the algorithm and to execute the algorithm itself. The iterative process itself is simply a loop directing repeated execution of the algorithm until terminal conditions are achieved. Each step in the iterative process brings the result closer to the stable solution, a solution whose amplitude is neither growing nor decaying over time. This is achieved by varying V_r and A* simultaneously. Each iteration entails a guess of these two values, being changed simultaneously, though not independently. After each calculation is performed, a new experiment is conducted if the stable solution has not been obtained.

The developed algorithm is completely autonomous, requiring only the input conditions to begin searching for a solution. Fig.9 shows the specific functions developed to implement the algorithm. These functions are described in Section 3.5.

3.3 Physical System Components

As the algorithm requires experimental inputs, a test rig is required to generate those inputs. This section details the physical components of the test rig, their installation and their function. The primary components of the system are shown in Fig.5.

Fig.6 shows the specific components of the test rig used in this thesis.

A water tank is used for conducting the forced motion experiments. The tank is located within the Sheets Ocean Engineering Building on the URI Bay Campus and has a total length of 3.5 meters and a useable length of 2.6 meters, with a useable depth of 0.68 meters (A). This carriage is attached with four free running wheels and four interior wheels on the sides of the tank which allow directed motion

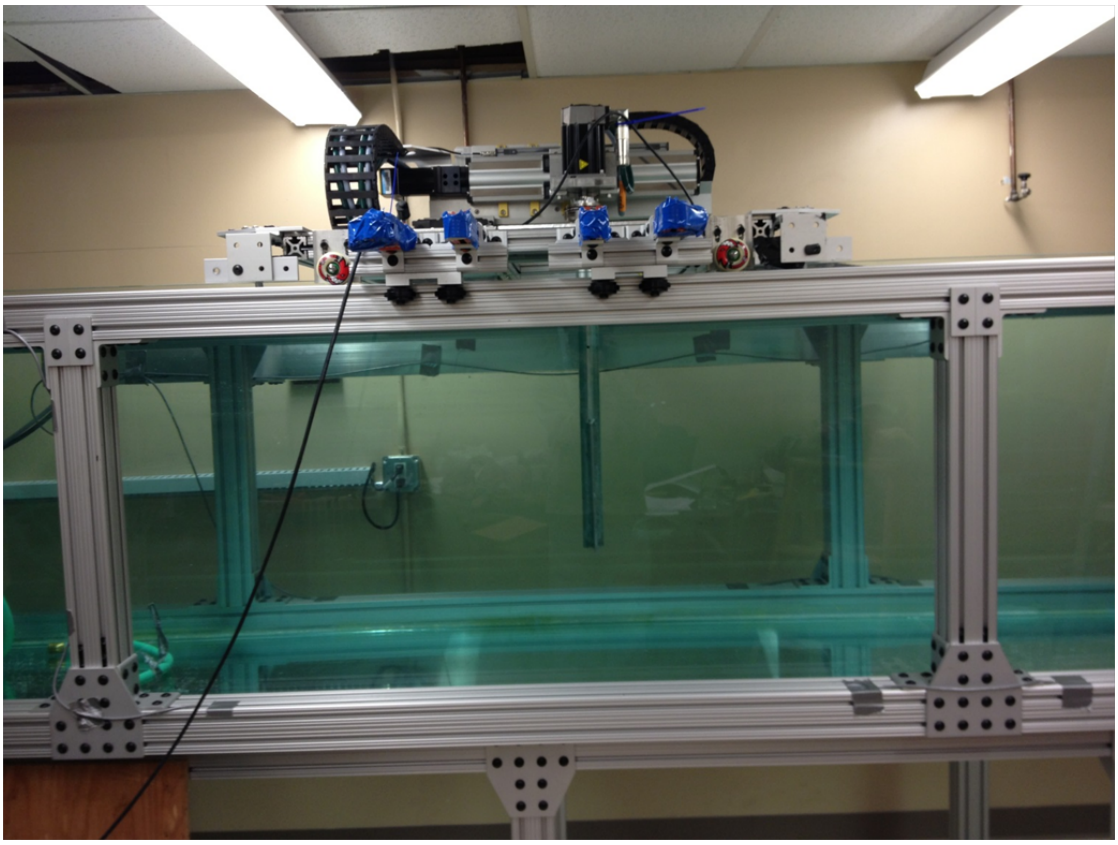

Figure 5: Image showing the experimental tank and carriage with a demonstration rig mounted.

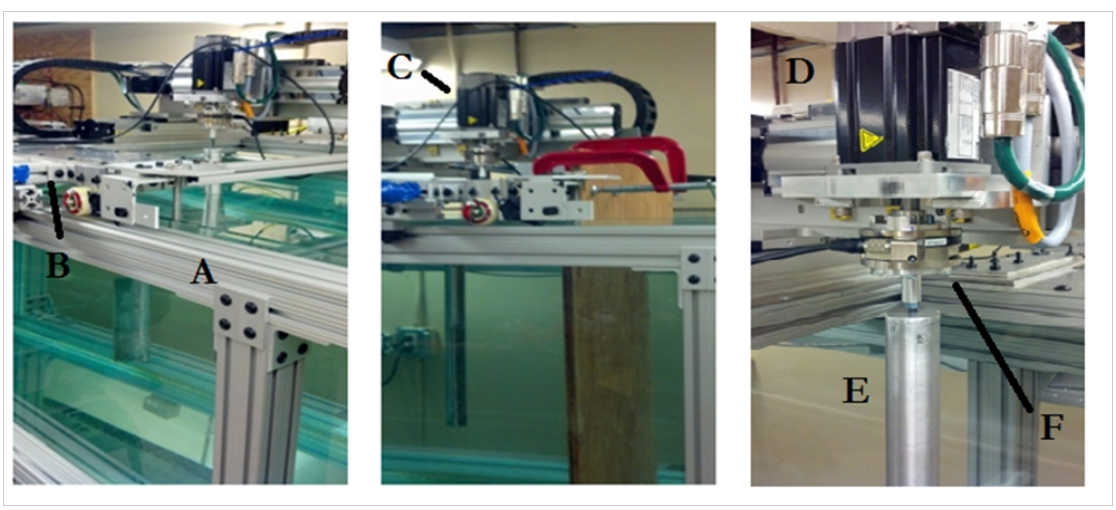

Figure 6: A selected set of views of the experimental apparatus under construction.

along the length of the tank (B). The carriage path is not perfectly straight due to deflection of the tank walls when the tank is full of water, but at less than a cumulative 9mm of 'bowing' between both sides of the tank, the level of introduced error to the straightness of the course is minimal. The carriage itself has three motors mounted (C). Two of the motors form a fine control X-Y axis, allowing linear motion in the X-Y directions. The final motor is the Z-axis rotational motor (D) which directly drives rotation of the mounted force sensor and test rig (a cylinder at – (E)). The Z-axis is not used for forced motion testing in the present study, however it is used for aligning the force sensor.The final component is the six-axis force transducer that the cylinder is mounted upon (F), a necessary requirement for recording all loads experienced by the test cylinder.

The six-axis force transducer is a Gamma sensor from ATI Industries and can record forces in the +/-130 N (newton) range in three axes: X, Y, and Z. It can also record three torques to a maximum of +/- 10 N-m (newton-meters). In both cases the force sensor is extremely sensitive to damage, though in principle failure will only occur at forces and torques greater than these figures by an order of magnitude. This safety margin allows forces to be recorded right up to the limit permissable within the accurate recording range of the force sensor, and the selection of test cylinders for the experimental apparatus was made with the objective of generating forces as close as possible to the upper range of the force sensor.

A four point mounting piece connects the test cylinder to the force transducer. This mounting piece is engineered as a quick-change interface so that different cylinders can be switched between a test series to allow for the new series to accommodate a different Reynolds number. Cylinders are positioned with a smooth plexiglass bottom cap within the desirable range indicated in Morse et. al.

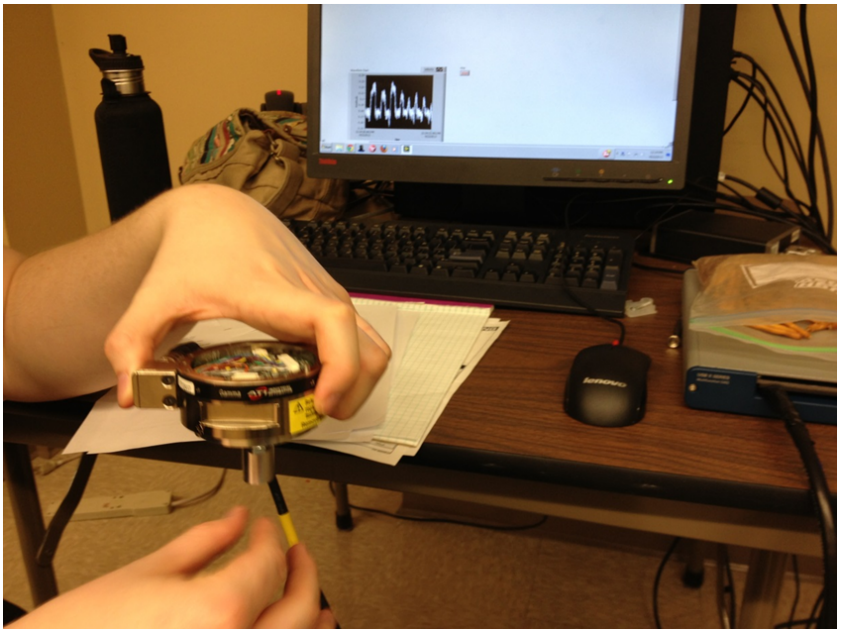

Figure 7: The force sensor being tested during installation with its output shown on the screen behind.

(Morse et al., 2008).

In addition to the issues that required the design of the special mounting piece, interference was discovered to be a serious problem with the force transducer during the testing phases and some early unrelated uses of the experimental system. As a solution, the DAQ system was isolated from the circuits providing power to the servo motors to eliminate the source of interference: noise passing through the building ground. To completely solve the interference problem, the installation of nylon machine screws for mounting the force transudcer through a rubber isolation pad guaranteed that the DAQ and force transducer were appropriately electrically isolated from the servo motors' power supply.

The Parker electronic motors are controlled via a Delta Tau UMAC Turbo PMAC robocontroller, which interfaces with the motors via Xenus drives. This Delta Tau robocontroller interfaces with a Lenovo desktop to control the function of the motors and allow for download of motion programmes which are then ex-

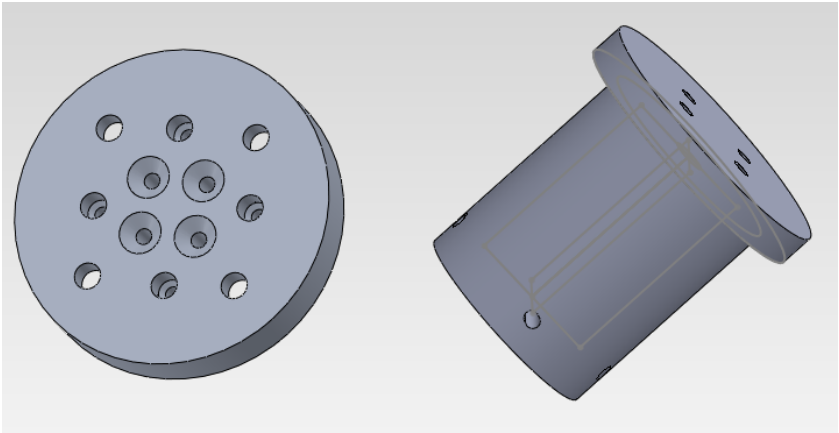

Figure 8: SolidWorks models of the quick-change mount attached to the force transducer and the test piece interface mount for a 1.5-inch outer diameter VIV test cylinder.

ecuted by the Delta Tau robocontroller. The force sensor's orientation is homed by using the Z-axis motor. This is done by use of a laser position limit sensor, which activates to lock the motor in place when the sensor is correctly aligned by interruption of the laser beam with a metal rod inserted into the side of the force sensor mounting piece.

3.4 System Control Components

The control components of the system comprise the mechatronics of the test rig and systems for recording, processing, and transferring data. The table below lists the Matlab Functions for use in this thesis. Section 3.4 generally describes how these functions interface with the experimental system hardware and section 3.5 describes how these functions operate as software in the implementation of the prediction algorithm.

Subsequently, it is necessary to outline a second table explaining the hardware/software components of the system, so that they are available for reference for a detailed explanation of the functions.

The interface between Matlab, as the base software controlling implementation

Matlab Function	Intended Purpose
Central Control Function	Overarching control of all functions and integration routines
Offset Correction	Purpose: to zero the force measurements.
PMAC working programme	Writes PMAC motion files
Download programme	Primary communication with Delta Tau Robocontroller for sending and execution of motion programmes, motor reset, and jog commands.
Gather Data	Secondary communication with Robocontroller for retrieving recorded position-actual data from the motors during the motion sequence
Coefficient Finder	Collates, filters, and processes data to obtain force coefficients based on the previously commanded motion.
Selection Analyzer	Runs the simulation of the cylinder in a free stream using the Newton Method to determine the variables for the next iteration of the system

Table 3: List of Matlab Functions in Simulation System

of the algorithm, Labview, used for data acquisition, and the PMAC programming language of the Delta Tau Robocontroller, is described in the following section. Matlab is used for central control of the algorithm. Delta Tau uses the PMAC motion-control language, a proprietary version of a machine tool programming language, to execute motions powered by electric motors according to pre-written programmes referred to as "motion files". A function was developed in Matlab called the "PMAC working programme" to generate a motion file based on the following input parameters: Amplitude, frequency, and flow speed (velocity). Amplitude and frequency are dimensionalized from A* and f* respectively. The flow speed is set as an initial system parameter to obtain a constant Reynolds number for a set of experiments.

The motion file, when uploaded to the controller, generates a sinsusoidal

Component Name	Function	Interfaces
Delta Tau UMAC Robocontroller	Execution of Motion Programmes, recording position data, system timing cues.	LabView DAQ 2, Motorcontrollers, Positioning sensors, control computer.
Xenus Drives/Parker Motors	Drives translate digital commands into analog control impulses for the motors; they were pre-integrated with motors.	Robocontroller
LabView DAQ 1	This DAQ collects the force sensor data, and must be electrically isolated from sources of interference.	Force sensor, control computer, LabView software.
LabView DAQ 2	Receives timing impulse from Robocontroller. Had to be separated from DAQ 1 for interference minimization.	Robocontroller, LabView software.
LabView Software	LabView is a visual bloc based programming language; a written programme records the force data.	DAQ 1, DAQ 2, writes to text files.
Matlab	Contains central control function, functions for writing motion programmes, sending commands to Robocontroller, obtaining force data, processing data.	All.

Table 4: Separate System Components

motion in the Y axis and a steady forward velocity with ramping acceleration/deceleration at the beginning and end of the test run. To upload the motion file to the controller through Matlab, the Gather Data function developed by M.L. Norg of Norg Consulting, dated to 2011, was modified (Norg, 2011). This function uses either a serial cable interface or an ActiveX COM interface to communicate between Matlab and the Delta Tau UMAC Robocontroller. These Matlab functions were also adapted and modified for data gathering from the controller in order to log the motor position. The function takes hexadecimal data through a serial transmission from the controller and translates it into ASCII format. An ActiveX COM interface was successfully implemented for communicating with the

Delta Tau UMAC. This interface allows for the passing of command calls from Matlab directly to the Robocontroller, including uploading the motion programs to the Robocontroller and calling them for execution.

Data acquisition of the force sensor is controlled by a VI in LabView. LabView is run in Matlab by executing a DOS command inside of the central control function in Matlab, and arranging the default settings for the vi which records the force sensor data to automatically turn on at program start. A similar command is used to stop the VI when not recording data. Data recording is triggered by a software switch included in the motion programme, which triggers a digital switch recorded by the DAQ 2 within the VI. This allows for rough alignment of the force and position data acquisition. Due to timing inconsistencies with the DAQ system and controller, further time alignment of the force and position measurements is performed in the data processing routines by measuring the carriage position and carriage velocity independently. Collected data is written to a text file which is then read into matlab and saved as a matlab database file (mat file).

Motion programs are written inside of Matlab, and sent to the Delta Tau UMAC Robocontroller, and then ordered to be executed. There is limited feedback, however, with no functionality to indicate to matlab when the motion program has finished executing in the Delta Tau, so trial runs had to be done and stop-timers to hold execution of the programme implemented to give enough time for all portions of the programme to execute in successfully before proceeding to the next portion. This could have been done using switches in the motion program, however, the present method only adds a few minutes to each iteration and this wait time is necessary to allow the tank water to settle anyway.

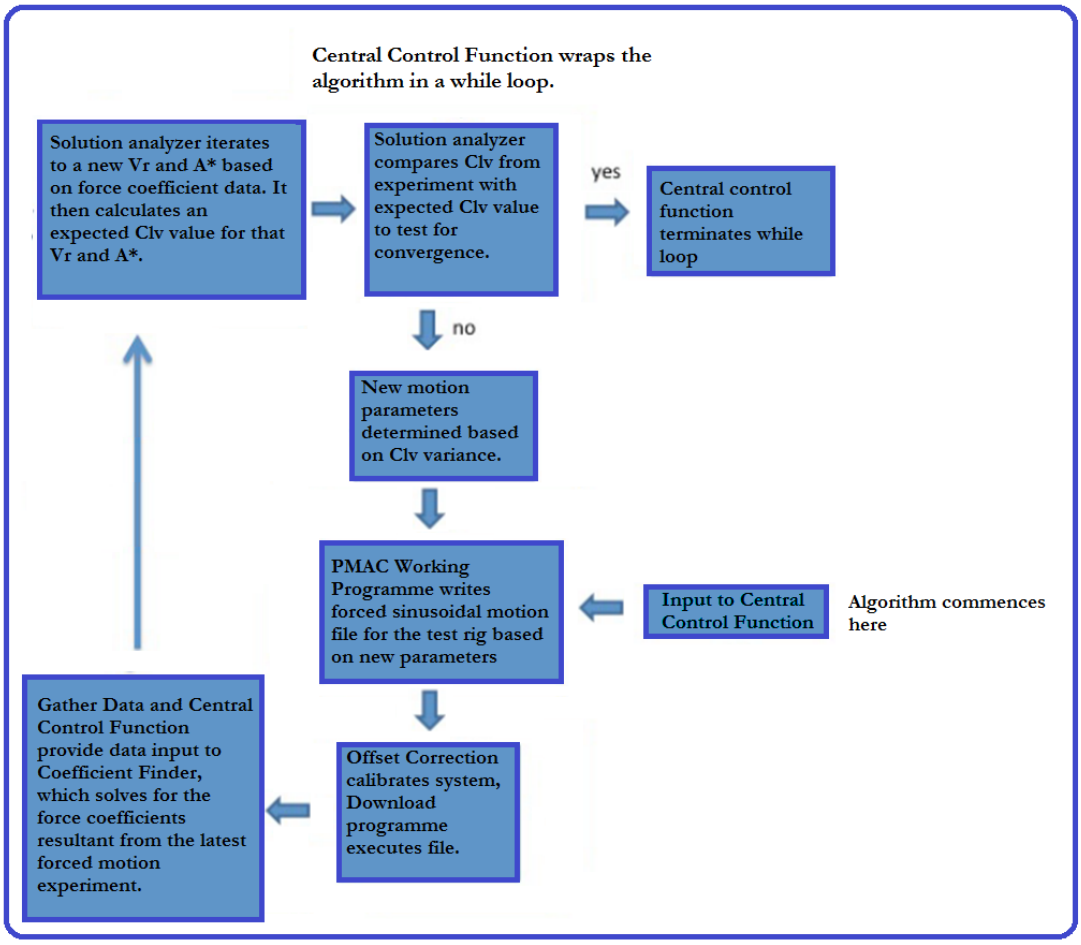

Figure 9: Flow chart showing Matlab Functions

3.5 System Functions

An outline of the programmes developed for implementation of the prediction algorithm are given in table 5, and their interaction with system components is covered in table 6. Details of the programmes are explained in the following section. These functions serve to integrate the physical system components and non-matlab programmes. Collectively they *are* the algorithm.

3.5.1 Central Control Function

The flow chart demonstrates how the matlab functions in which the algorithm is implemented relate to the basic concept of the algorithm in the abstract. The

Central Control Function serves to control all aspects of the system operation. A while loop is used to control iterations of the system, with the loop continuing to iterate until the convergence criteria has been met. The convergence criteria is an output from the Selection Analyzer program and a description of different convergence criteria used is given in that section.

The Central Control Function receives the initial conditions for the simulation, the initial conditions for the test rig (describing its present configuration for the set of runs to be conducted), and the initial A* and V_r values for the first experiment that commences each iteration. These values are tabulated in a header file called VIV Prediction Wrapper. This is a simple matlab script intended to be edited to reflect changing simulation parameters and changing test rig configurations. It accepts the variables, and sends them to the Central Control function, calling the function so that it begins to execute. The table shows only the variables used in the current iteration, other variables can be commented out or used, depending on available data for the simulation.

After being called by the VIV prediction wrapper, the Central Control function takes the inputs, performs basic calculations from them to provide appropriate variables to the other functions, and then passes the output variables from other functions, and data arrays from function to function, calling the functions at the appropriate times, and writes data to database files.

3.5.2 Offset Correction function

The Offset Correction functionrecords force data to zero the force sensors. It is derived from the Download programme function. It relies on the method demonstrated by Norg (Norg, 2011) for using an ActiveX COM interface between matlab and the Delta Tau UMAC Robocontroller. In the case of the Offset Correction function, it simply activates the motors and sends the appropriate M-variable

Variable	Description
testcyl_mass	Mass of Test cylinder
test-cyl_conn_mass	Mass of test cylinder connector
force_conn_mass	Mass of connector to join force transducer to test cylinder connector
diameter	Diameter of experimental test cylinder
L	Submerged length of experimental test cylinder
sampling_f	Sampling frequency for LabView DAQ board (force measurements)
kine-matic_viscosity_test	Viscosity of experimental test fluid, $\frac{m^2}{s}$
AMP	Initial non-dimensional amplitude guess for solution
zeta_mstar	Structural damping coefficient times mass coefficient for simulated cylinder
dia	Diameter of simulated cylinder
density	Density of fluid
kine-matic_viscosity_sim	Viscosity of simulated fluid, $\frac{m^2}{s}$
ustar	U*. Nominal reduced velocity for simulated cylinder during the current iteration sequence.
folder_name	Folder you save data to (must be created by user).
u	Velocity of current run.
Vr	Vr for cylinder, initial guess.

Table 5: Options for the VIV Prediction Wrapper

command to begin logging data in LabView, which is turned on and off before utilization of this function to properly record the data, from within the Central Control Function. The function turns the motors on, holds them on, and then turns them off after enough data has been logged by the force transducer via the DAQ VI to apply the offset correction. Data is logged to a text file and then saved in the central control function.

3.5.3 PMAC Working Programme function

This function uses modified, pre-existing programmes to write an ASCII file with a PMAC motion program or multiple PMAC motion program which may

then be uploaded to the motion controller. This program uses inputs defining the motion of the cylinder–dimensionalized amplitude, dimensionalized frequency, and carriage tow velocity, and writes a set of Position-Velocity-Time intercepts to define the desired motion of the test cylinder. Each discrete time PVT block has a set time at which the motor should reach that position, and velocity at that position and time; and a set time and position at the end of the move, as well as velocity the motor is to possess at the end of the move. However, the velocity *within* the move is *not* fixed, the motorcontrollers calculating their own required velocity, which may vary, to meet the end constraints when leaving that block and passing into the next. The motor controller ensures that the contraints are met, with the result being a sufficient digital approximation of a sinusoid with high positional accuracy. The number of discrete points defining the motion is a programmable variable. The motion is harmonic as in the following equations:

$$y = Acos(\omega t) \tag{15}$$

$$v_y = -A\omega sin(\omega t) \tag{16}$$

Where A is the dimensionalized amplitude, $\omega = 2\pi f$, and f is the dimensionalized frequency. The carriage velocity is programmed based on a trapezoidal function. Three cycles of motion in y are performed before moving the carriage to minimize transients in the force measurements.

3.5.4 Download Program function

This function sends commands to the Robocontroller directing it to download the motion programs file written by the PMAC Working Programme function, activates the motors, and commands the Robocontroller to execute the motion programme. The Download program function includes a jog command to return

the carriage to the rest position at the 0-point end of the tank and motor resets in addition to the execution of a series of programs for homing, followed by the actual motion programme.

3.5.5 Gather Data function

Gathering data is the last of the basic coordination and command functions. Based on the modified program from Norg (Norg, 2011), it takes hexadecimal actual position data gathered from the motors by the Delta Tau Robocontroller, parses it, and translates it into U/X/Y/Z (as required) positions based on motor counts. These data are reproduced in column format with a separate time column. It should be noted that the sampling frequency of the position may vary based on the number of channels to be gathered and the available memory in the controller gathering buffer. The Data Gather function will determine the sampling frequency used based on the controller settings. These data are passed into the central control function and written for record into the database.

Gathered data measures the *actual* rather than commanded position. A sample plot of the output is provided in Fig.10.

3.5.6 Coefficient Finder

A critical part of the system methodology is how the force coefficients are calculated. Two types of data are measured to solve for the force coefficients: Position data, and force data. The position data include the actual position, velocity and acceleration of the cylinder as opposed to the commanded kinematics. Force data include all forces and moments exerted on the cylinder. In order to isolate the hydrodynamic forces exerted on the cylinder, the inertia of the test cylinder must be removed from force measurements. This is done by measuring the mass of the test cylinder and the acceleration of the cylinder to determine

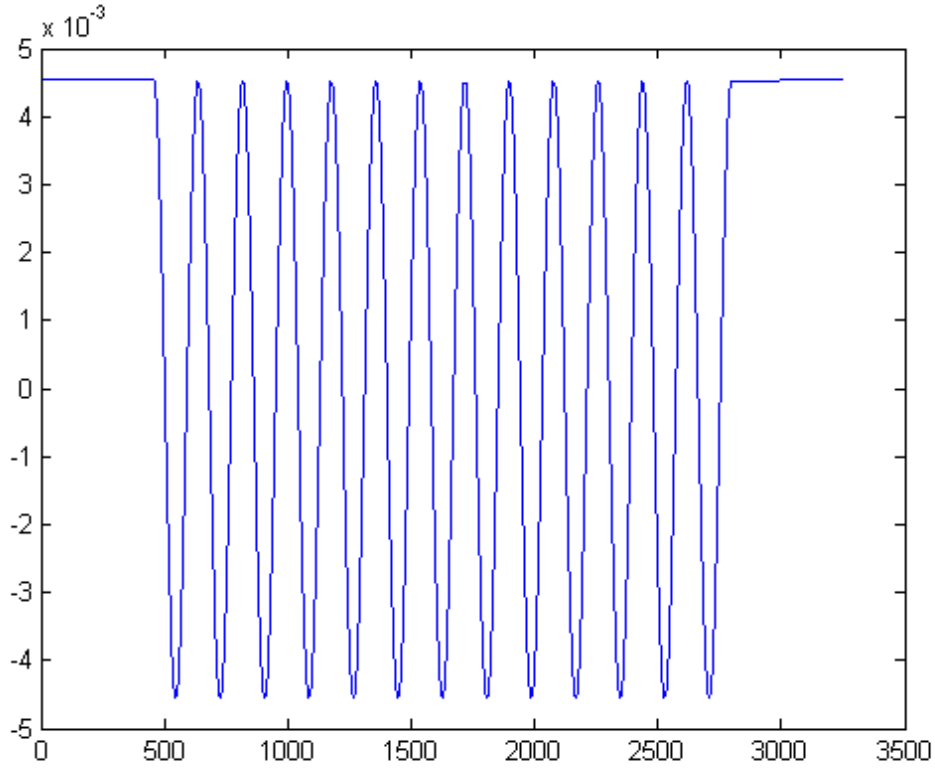

Figure 10: Actual position data, showing retrieved Gather Data

the cylinder's inertia. This inertia is subtracted from the total force measured in the direction of motion, leaving only the hydrodynamic force. Then velocity and aceleration are determined by taking the derivatives of position. The force primarily used in these experiments is the lift force, or force perpendicular to the current. The force and position signals are trimmed to only include data when the cylinder was in forward motion after any initial transients have died out.

The Coefficient Finder takes both the position data (converted from hexadecimal to ASCII data files) and the force data (recorded by LabView into ASCII data files), trims and filters the data, aligns the data in time, and calculates force coefficients for the particular commanded motion. The force sensor data is calibrated using a six-axis calibration matrix supplied by the force sensor vendor. The calibration matrix was verified by applying known loads to the test cylinder and measuring the resulting voltage outputs from the sensor. It was found that the cantilever setup of the test cylinder results in a natural frequency of about 7hz, which can be observed in the force signals. This frequency is sufficiently above the expected measured force frequencies, such that it can be removed through filtering without appreciably degrading the force signal. Fig.11 shows the data as read into the function for aligning the force and position output:

Fig.12 shows the filtering process:

Fluid force and motion frequency are compared using FFT analysis. Assuming the fluid force is a phase-shifted sinusoid with phase ϕ , ϕ is calculated based on the relative phase difference between the position and lift force FFT, used to compute C_{Lv} and C_{La} in Equations 3 and 4. The magnitude of C_L may then be found through Trapezoidal numerical integration of the power spectral density. This provides the variance of C_L, C_{L_var}, such that the magnitude of $C_L$is found as:

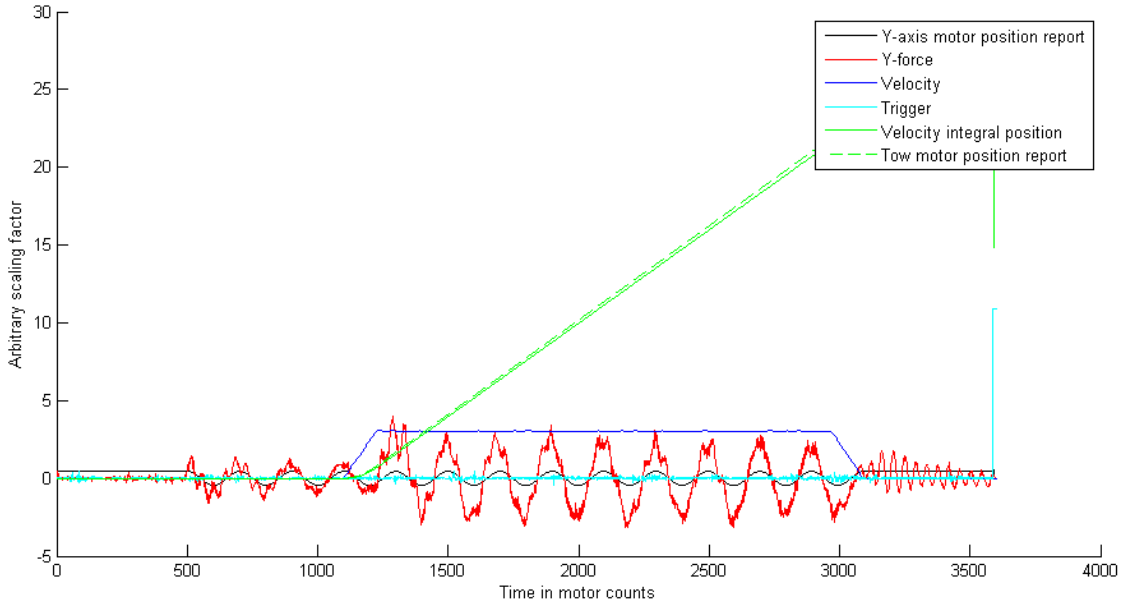

Figure 11: Green lines indicate change in position from the position and force datasets. Since these must be occurring at the same points in time, the two sets can have their positions (in iterations of data collection, i.e. sample points) correlated and normalized.

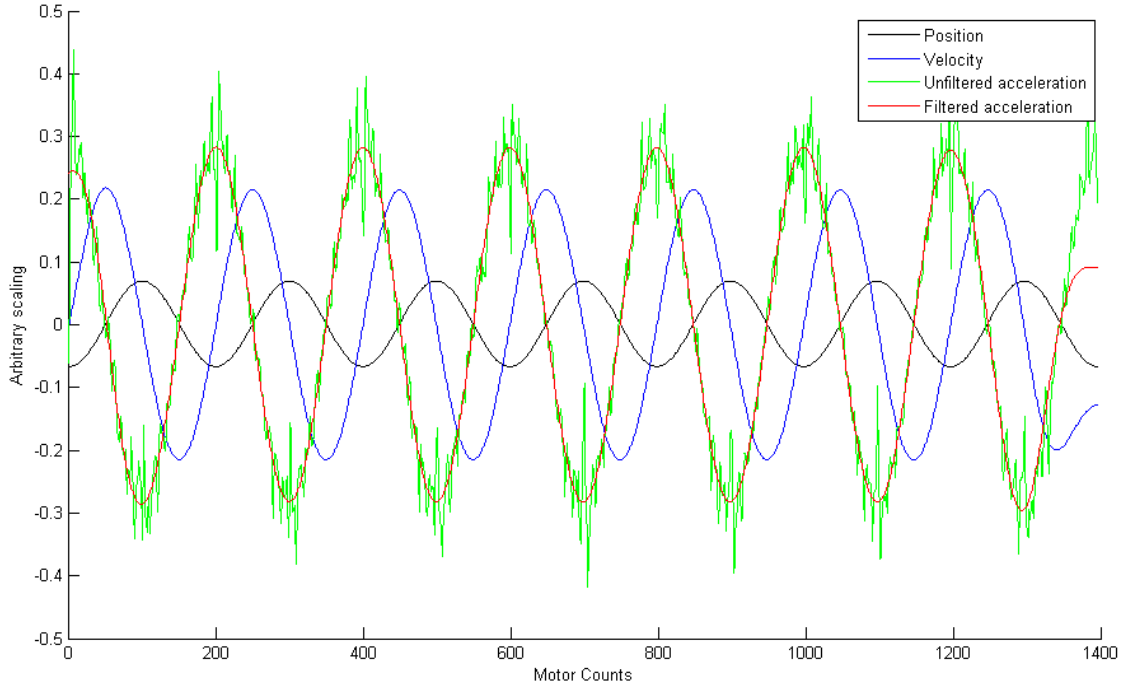

Figure 12: Filtering Process, quality of signal improvement.

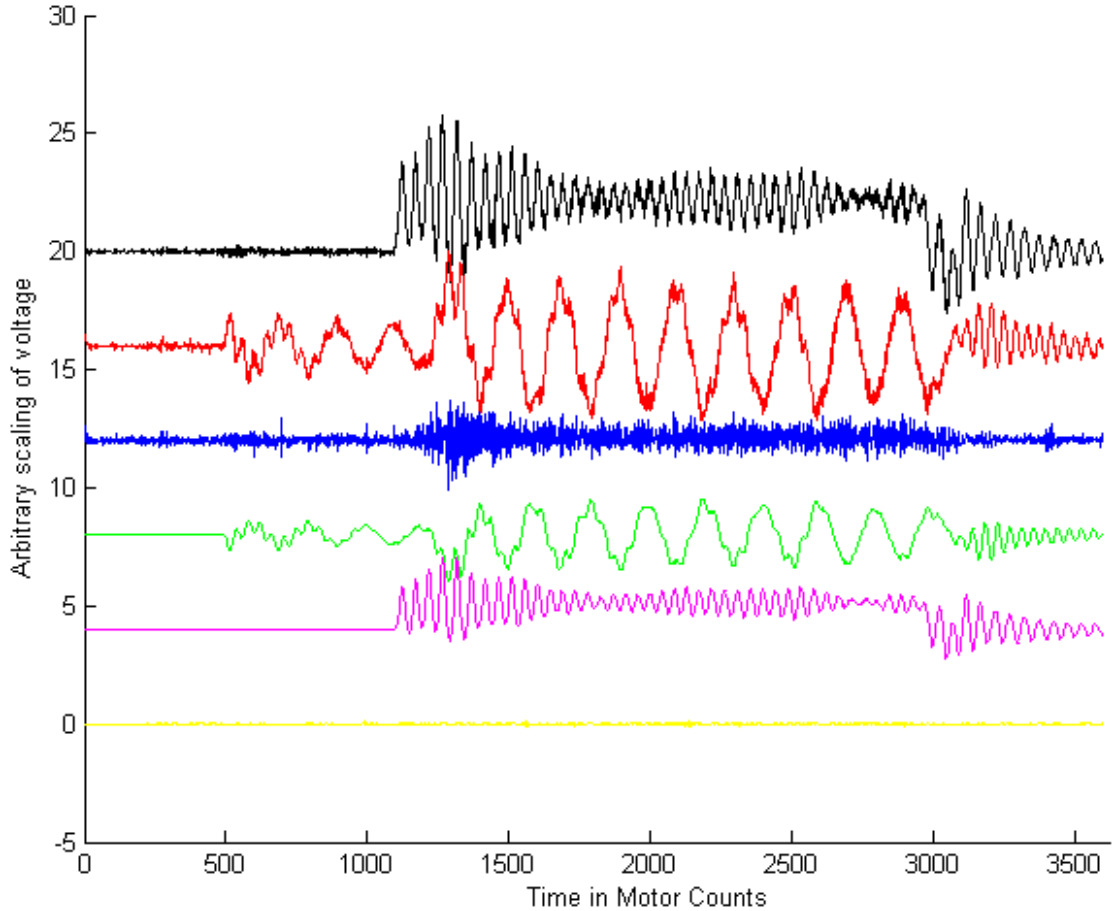

Figure 13: Raw force data from the six-axis force transducer as plotted upon its input to the Coefficient Finder.

$$C_L = \sqrt{C_{L_{var}}} \cdot \sqrt{2} \tag{17}$$

Using Equations 4 and 3, the calculation of $C_{Lv}$and C_{La} is simply based on $C_L$and ϕ . The added mass coefficient, C_M is then determined from Equation 18:

$$C_m = -\frac{(C_{la} V_r^2)}{2\pi^3 A*} \tag{18}$$

The resulting force coefficients are then passed on to the selection analyzer. A plot of C_L relative to the inertia of the system is provided in Fig.14.

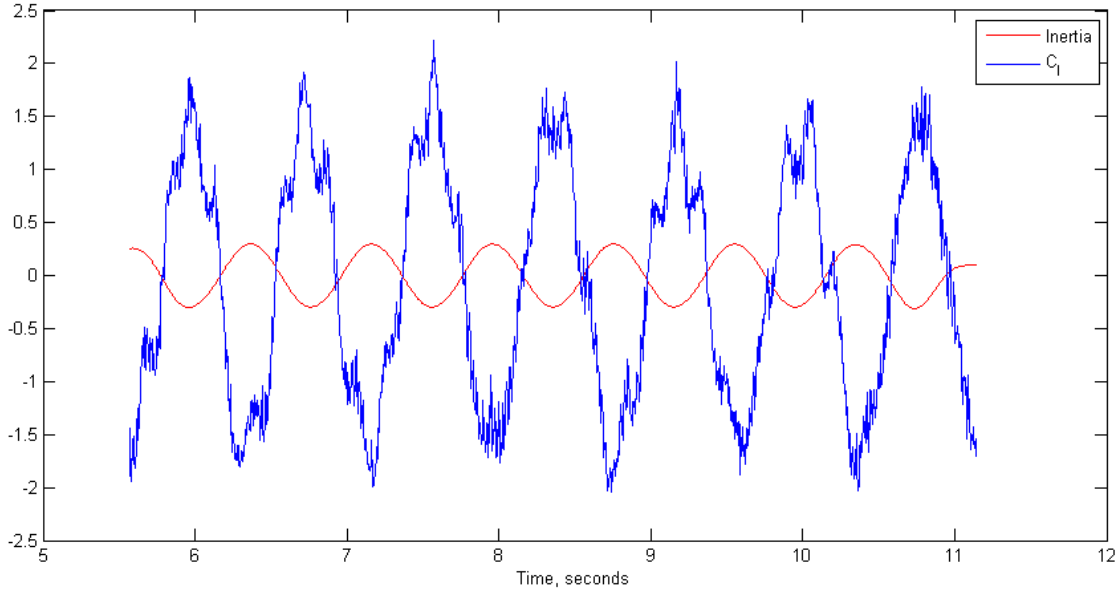

Figure 14: C_L plotted in blue and inertia plotted in red as a function of time

3.5.7 Selection Analyzer

The Selection Analyzer function uses a Newton-Raphson method which takes in the measured fluid force coefficients and determines the next best guess for $V_r$and A* based on equations 6 and 7. The Newton Function in this case takes the form:

$$V_{r\,new} = V_{r\,old} - \frac{G}{\frac{dG}{dV_r}} \tag{19}$$

Where G, determined by rearranging equations 6 and 7, and $\frac{dG}{dV_r}$ are defined as:

$$G = \frac{V_r}{U*} - \left(\frac{1}{1-\alpha V_r}\right)^{-\frac{1}{2}} \tag{20}$$

$$\frac{dG}{dV_r} = \frac{1}{U*} + \frac{\alpha}{2\sqrt{1-\alpha V_r}} \tag{21}$$

And α is a constant for each iteration that is a function of C_{Lv}. α can change with each iteration since it is dependent on A* and V_r through C_{LA} and C_{Lv}. This

Newton-Raphson method determines a new value for V_r with each iteration, but does not determine how A* should change with each iteration.

$$\alpha = \frac{2C_{La}\zeta}{C_{Lv}U*} \tag{22}$$

Rearranging equation 5 and taking C_L in phase with velocity, one can determine the expected value of C_{Lv} if A* and V_r are correct (which may or may not be true for a given iteration).

$$C_{Lv_{expected}} = \frac{4\zeta\pi^3 m * A*}{U * V_{r_{new}}} \tag{23}$$

Convergence of the algorithm would then require that the measured value of C_{Lv} approaches $C_{Lv_{expected}}$, such that ΔC_{Lv} is driven to zero:

$$\Delta C_{Lv} = C_{Lv} - C_{Lv_{expected}} \tag{24}$$

As ΔC_{Lv} will be nonzero if the algorithm has not converged, a new value of A* may be determined as a function of ΔC_{Lv}. The calculation for the new value of A* may then be made as the current value for A* is multipled times the resultant of $1 + \Delta C_{Lv}$. As a practical matter, however, the process runs into a problem, in that C_{Lv} may be greater than unity, leading to negative values of A*. To address this, based on the size of C_{Lv} a constant is used to reduce the size of the amplitude change to avoid the function commanding negative amplitudes. The equation for A* with the constant rendered as g, is shown in equation 25. The value of g varies from $\frac{1}{2.1667}$ to $\frac{1}{6.5}$ based on the maximum value of C_{Lv} for Re = 12000 from Morse and Williamson (2009). The values g may be varied as a function of the current calculated value of C_{Lv}.

$$A*_{new} = A * (1 + (g\Delta C_{Lv})) \tag{25}$$

The remaining portion of the Selection Analyzer defines the convergence criteria. Two separate methods were used for the convergence criteria. The first of these consisted of a calculation using equation 25 and arbitrarily defining convergence as an approach of the calculated new A* value to a difference not greater than 4% of the maximum attainable A* value in Morse and Williamson (Morse and Williamson, 2009), circa A* = 1.6, from the prior value of A*. This cumbersome and arbitrary method was replaced by a less arbitrary method based on C_{Lv}.

This method requires the difference between C_{Lv} and $C_{Lv_{expected}}$, to be $\Delta C_{lv} < 0.2$. This choice represents values of $< 4\%$ error in the converged value for the amplitude. This error is inherent in the current system due to limitations on the signal to noise ratio of the force sensor. Improved resolution of the force sensor or a reduction to the test cylinder inertia, or an increase in the test flow speed, may allow for this criteria to be reduced in the future. However, because convergence can be expected only at positive values, $C_{lv} > -0.1$ is also set. This is because a convergence at a negative C_{lv} is a *true* error (there is no possible way for convergence to a stable case of VIV to occur at negative values of C_{lv}) and should be more strictly limited than at positive values where the multiple overlapping branches mean multiple convergences at a single value of V_r. The Analyzer function returns a successful output and value that terminates the while loop if the convergence criteria are successfully reached. If not, the new V_r and A* are used as the basis for the variable inputs in writing a new motion programme for the next iteration of the while loop in the Central Control Function, and the loop continues while the Newton Function progresses toward a stable solution of the simulation.

CHAPTER 4

Results and Analysis

Results obtained from the developed algorithm are compared to documented free vibration experiments. Chosen experiments for comparison include Khalak and Williamson (Khalak and Williamson, 1999), Gharib (Gharib, 1999), Vikestad (Vikestad et al., 1997), and Smogeli (Smogeli et al., 2003). Khalak and Williamson and Gharib shared multiple features. They both used vertical cylinders, and had Reynolds numbers from 10,000 - 25,000; in its present configuration the test rig is limited to an Re = 5500 - 16500. The Khalak and Williamson (Khalak and Williamson, 1999) dataset used m* = 2.4 and ζ= 0.0058, and the dataset from Gharib (Gharib, 1999) had m* = 28, ζ=0.0070, allowing for dramatically different m* to be simulated in the present study. The Khalak and Williamson experiments were for a fixed Reynolds number and the Gharib experiments were for a variable Reynolds number. In both cases there was no attempt to match the Reynolds number exactly, which has led to some error, however Reynolds numbers were similar.

In the cases of Vikestad (Vikestad et al., 1997) and Smogeli (Smogeli et al., 2003) datasets involved variable Reynolds numbers, including Reynolds number values of up to Re = 40000. Additionally, both systems used horizontally suspended cylinders for their free vibration experiments, as opposed to vertically mounted cylinders as in Khalak and Williamson (Khalak and Williamson, 1999), Gharib (Gharib, 1999), and the present simulation system. The particular dataset was chosen from Smogeli (Smogeli et al., 2003) for conditions m* = 4.0, ζ=0.0094, and from Vikestad (Vikestad et al., 1997) for m* = 1.277 and ζ=0.00147.

Generally, the objective in all runs was to reproduce the basic shape of the data as closely as possible. A range of U* values were selected as inputs to the algorithm, with the spacing of values varying from U* = 0.05 - 0.5; this allowed an increase in number of points around the anticipated hysterisis on the expectation that these locations would require an increased number of data points to properly determine the amplitude.

The algorithm was run with the objective of producing at least 20 data points for comparison with each data set from the literature, for approximately 80 points. Each point entailed between one (for several cases where the initial points guessed were close enough to the convergence criteria) to eighteen test runs being conducted. Convergence was highly dependent on the magnitude of C_{lv} and was more difficult to obtain in regions with low C_{lv} values. In all, the system produced good results for approximately forty full system iteration loops, completely reproducing the experimental data from two cases, each of a different prior study. Two other more dissimilar systems attempted did not yield good results, and the reasons for these outcomes are also discussed.

4.1 Validation of experimental setup

To validate the experimental setup, single forced motion experiments were performed and the resulting hydrodynamic force coefficients were compared with equivalent experiments from Morse and Williamson (Morse and Williamson, 2009) and Gopalkrishnan (Gopalkrishnan, 1993). This was done by commanding a single experiment without the full loop, and comparing the values of C_M and C_{Lv} which resulted from the experiment with data from prior forced motion studies. Once a few initial results yielded correct outcomes, a total of twenty-five more comparisons were performed. These points were compared with Morse and Williamson (Morse and Williamson, 2009) at Re = 12000 and Re = 4000. The

second source was a thesis by R. Gopalkrishnan (Gopalkrishnan, 1993) which also contained forced motion data for these coefficients at Re = 1300. Some error exists due to slight differences in Reynolds numbers, so a comparison $\Delta C_m < 0.2$ and $\Delta C_{Lv} < 0.2$ was deemed sufficient to verify correct free measurements.

Good comparisons exist for C_{Lv}, with all of the cases tested producing reasonable results. A complete table is reproduced in Appendix A; a select subset is shown in Table 4.1. These values were compared to manually plotted points on the Morse and Williamson (Morse and Williamson, 2009) and Gopalkrishnan (Gopalkrishnan, 1993) graphs and verified to be within the $\Delta C_{Lv} < 0.2$ limit for error in comparison to the C_{Lv}value for the given value of A*.

actual A*	C_{Lv}
0.2	0.233
0.4	0.0463
0.6	-0.2
0.8	-0.538
1	-1.08

Table 6: Selected C_{Lv} test values at V_r= 6.76.

Good comparisons ($\Delta C_m \leq 0.2$) exist for C_m except for 6 cases out of 25. Two different identifiable problematic regions occurred with the C_m data points. The first was for A* = 0.8 - 1.0, V_r= 10. At these two points C_m was of the correct sign but approximately twice the expected magnitude. The second was for the case of A* = 0.2-0.6, V_r= 3.39-3.95. In this region C_m possessed the correct sign but the magnitude was off by a margin greater than that considered acceptable, a $\Delta C_m \sim 0.4$ for all four of the points in question, in each case being *greater* than the expected result, and never less than the expected result. For the first set of points at a very high reduced velocity (V_r˜10), it is likely that the wake won't even synchronize for the given region, making comparisons and results dubious, though this could not be tested without a large number of cycles or visualisation of the

wake during the test. For the low reduced velocity (V_r~3.3-3.95), the discrepancies occur for high frequency motions with low amplitudes. In these conditions the inertia will be large, while the fluid force may be relatively small. This might just be an inherent error in the test rig which would only be alleviated with a lighter cylinder, more sensitive force sensor, or better modeling of the inertia force. Since the values *do not affect convergence in a measurable way,* the C_m errors could be regarded as acceptable for the objectives of this system.

4.2 Initial simulation attempts

Vikestad (Vikestad et al., 1997) and Smogeli (Smogeli et al., 2003) comprise the cases reviewed herein. In both cases the datasets involved variable Reynolds numbers, including Reynolds number values of up to Re = 40000, and horizontally instead of vertically suspended cylinders as in Khalak and Williamson (Khalak and Williamson, 1999), Gharib (Gharib, 1999), and the present simulation system. These datasets encountered problems which require discussion.

4.2.1 Comparison with Smogeli.

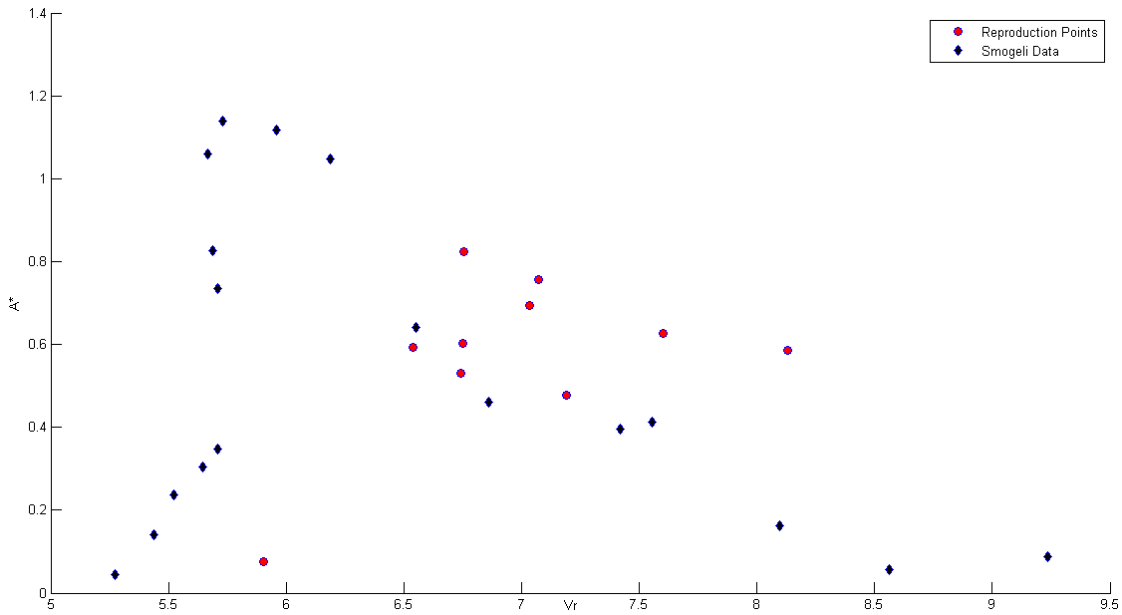

Figure 15: The results of an attempt to reproduce the Smogeli data, overlaid in red triangles from the original plot and re-projected to scale.

The results from Smogeli (Smogeli et al., 2003) were only partially reproduced, as shown in Fig.15. For the middle range of V_r response amplitudes are comparable, however at high V_r the simulation overpredicts the response. At low V_r, the simulation was unable to derive a response, hence comparisons cannot be made; the simulation also did not capture the high amplitude response at $V_r = 6$. This problem is most likely related to Reynolds number discrepencies or correlation length.

4.2.2 Comparison with Vikestad.

In the case of Vikestad (Vikestad et al., 1997), the shape of the response curve is captured by the simulation, however the A* curve looks to be shifted, almost by a constant value. Fig.16 shows the measured response from Vikested compared with the simulation from the present study.

Knowing that A* is a function of Reynolds number per Govardhan and

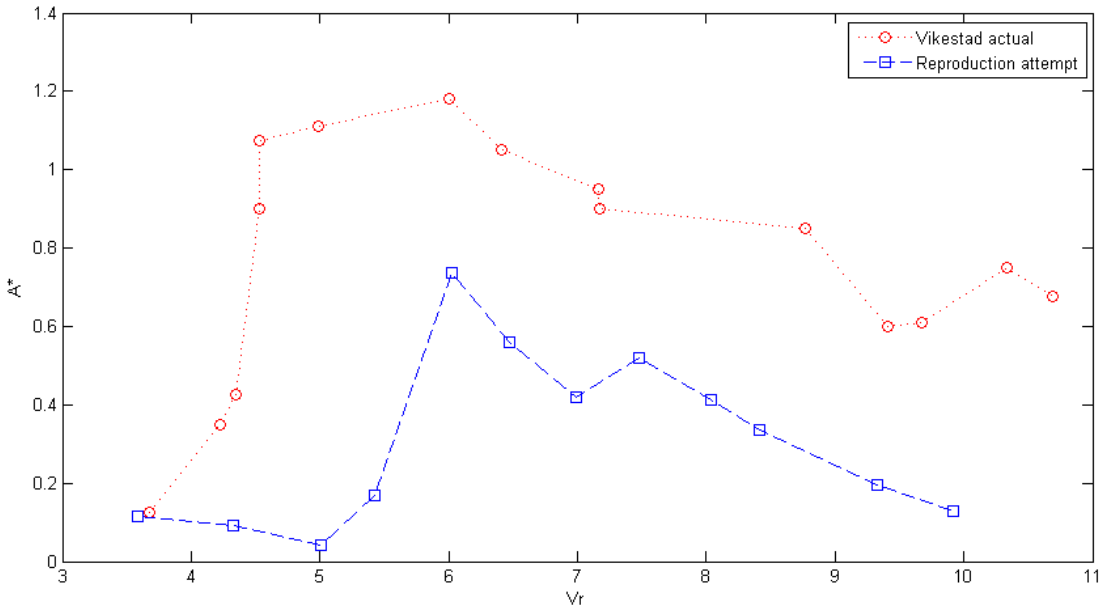

Figure 16: Vikestad actual data versus Vikestad reproduction.

Williamson (Govardhan and Williamson, 2006), an approximation to correct for Reynolds number is applied to account for the continuous variation in Reynolds number in the actual Vikestad results. The approximation improves the comparison, however, a large discrepency still exists, such that the argument that the varying Reynolds number across the range of V_r actually caused the different A* values cannot be sustained.

The results are clearly improved by showing closer normalized A* values across the range of V_r, but does not yield comparable values for A*. For further comparison, however, both the original Vikestad data and the reproduction attempted were plotted across the Morse and Williamson (Morse and Williamson, 2009) forced motion results for Re = 12000, with the original Vikestad (Vikestad et al., 1997) data being normalized to a fixed Re = 16500, in the inverse of how Fig.17 was modified to account for the changing Reynolds number in this original data. Thus, the plot shows how the Vikestad experiments should appear if run at a constant Reynolds number.

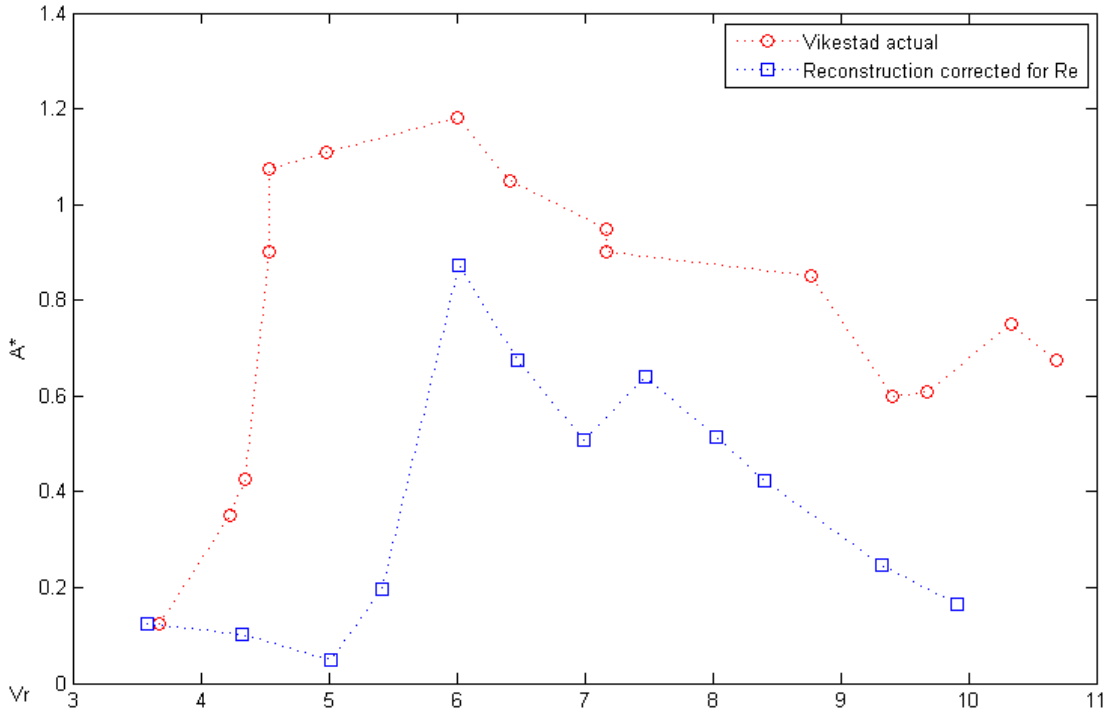

Figure 17: Vikestad reproduction attempt modified by approximation from Govardhan and Williamson (Govardhan and Williamson, 2006).

From these results it can be clearly seen that the convergence of Vikestad et. al. occurs in a range where according to Morse and Williamson (Morse and Williamson, 2009) it *cannot.*, whereas values for the reproduction attempt show convergence within an allowable range of error for C_{Lv}, bearing in mind that these results were conducted with the first and less precise convergence criteria. It must noted, however, that this graph is only completely applicable at Re = 12000, so successful convergence by Vikestad (Vikestad et al., 1997) is still probable; this outcome however demonstrates that precise matching of Reynolds number may be necessary for truly accurate results.

4.3 Comparison with Khalak and Williamson.

A good comparison was made with the free vibration experiments of Khalak and Williamson (Khalak and Williamson, 1999). These automated experiments

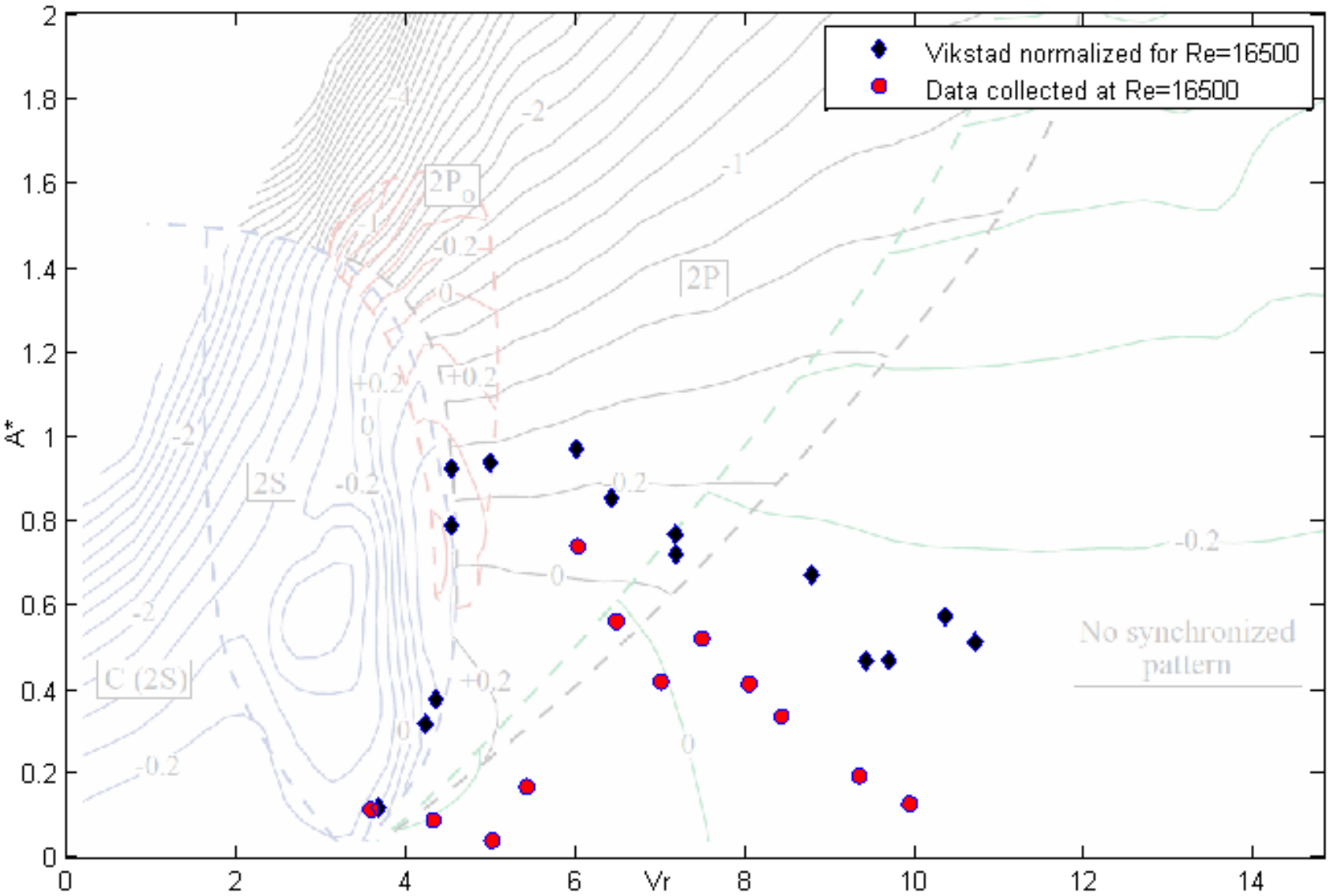

Figure 18: Vikestad normalized to Re = 16500 overlaid across Williamson forced motion plot for C_{lv}

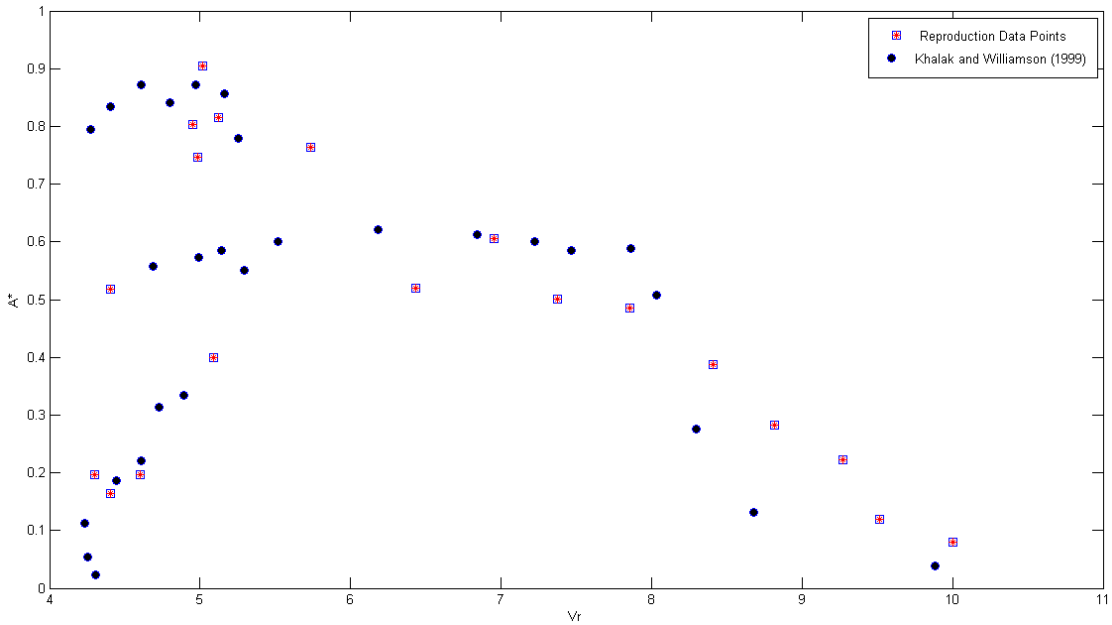

Figure 19: Reproduction points plotted over Khalak and Williamson (Khalak and Williamson, 1999) original chart.

used convergence criteria based on the final change in A* between two specific iterations of the loop being less than 4% of the expected maximum value for that *set* of runs. This value was selected on account that the system resolution would make additional precision in A* physically impossible. The expected maximum being the observed maximal A* value for the dataset being reproduced. At this point the system would conclude that convergence had been achieved. Two kinds of data were gathered. Firstly, the A* versus V_r data were compared by plotting against Khalak and Williamson's results. The attempt was made to most perfectly reproduce the m* = 2.4 case. Secondly, the C_{Lv} data were gathered and a mean difference in C_{Lv} is provided.

Fig.19 shows Nondimensional Amplitude, A* as a function of V_r, compared with the experiments of Khalak and Williamson:

Convergence between the Khalak and Williamson values and the attempt to reproduce them proved to be extremely good despite some issues with convergence,

where it was possible for the algorithm to choose a negative A* value. This problem with convergence was later addressed during experiments compared with Gharib (Gharib, 1999), where the convergence criteria was modified to be based on C_{Lv}, as described in section 3.5. This excellent convergence of results can be seen in Fig.19.

The simulation does not capture the full curve of Khalak and Williamson, due to the sparsity of simulation points, but the simulation does show clustered points at the low V_r, low A* branch, the upper branch, and the high V_r, lower branch. Some discrepencies exist at high V_r where the limited cycles of the simulation may not result in a perfectly synchronized wake. Nonetheless, three distinct branches are clearly shown and the maximum and typical amplitudes correspond extremely well.

For these data it should also be considered that an earlier and less effective convergence criteria was used. Despite allowing greater inaccuracy, the system at this stage was still very capable of reproducing these free vibration data points. Improvement of the convergence criteria shows significant improvement in comparisons.

Fig.20 is a convergence plot for these data. Each specific dataset shows lines connecting each point in the iteration, illustrating the convergence process as the system iterates through a series of experiments and converges on the correct answer. A very interesting trend in these data displays itself. At high values of V_r, large changes in V_r occur as the system attempts to converge. In the middle V_r values corresponding with the 2P wake, extremely large amplitude changes but small changes in V_r are observed as the system trends toward convergence. For the complicated wake region at low V_r values, both patterns of convergence occur.

Finally, C_{lv} values were also tabulated for the results of each converged point.

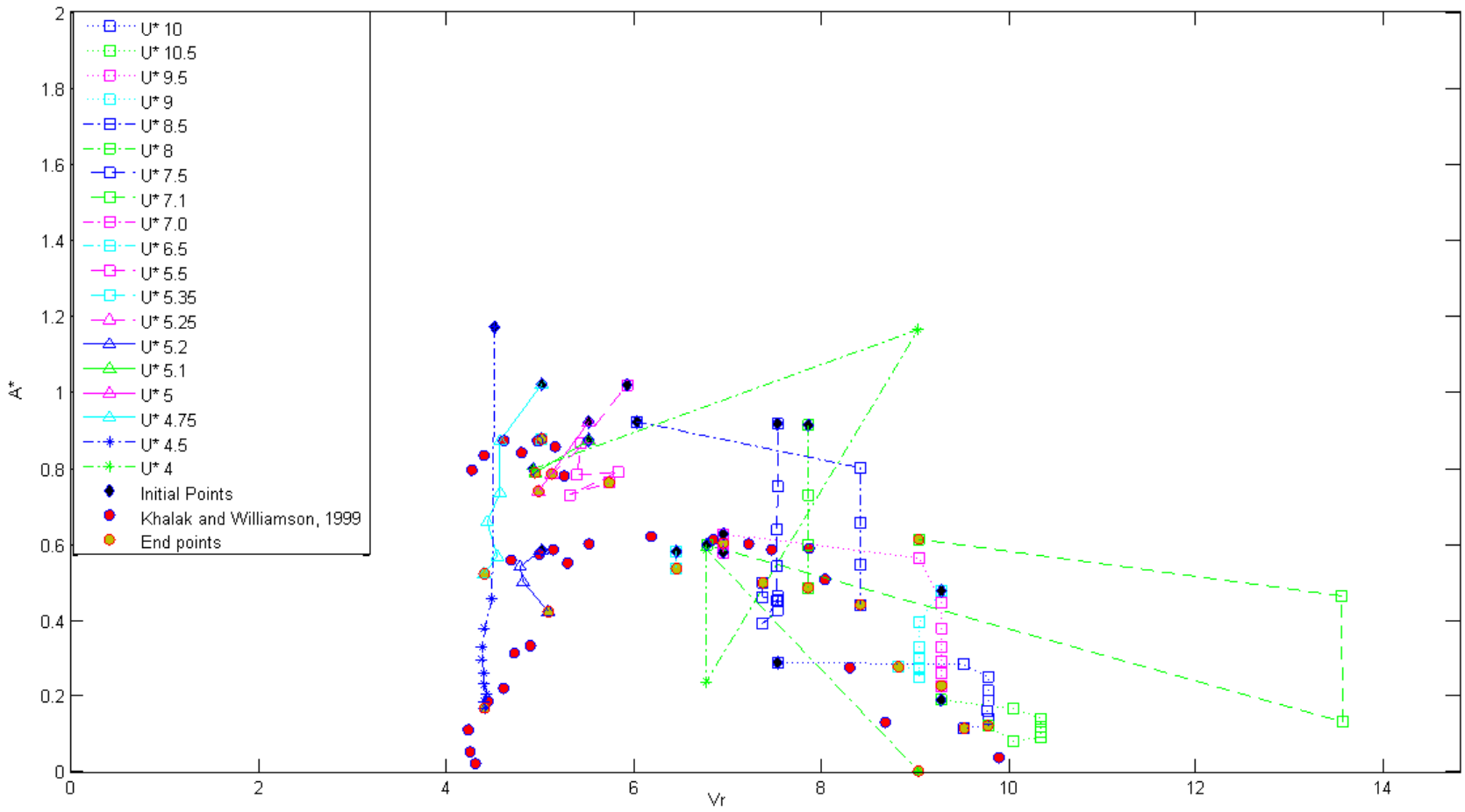

Figure 20: Convergence data for Khalak and Williamson reproduction, with Khalak and Williamson (Khalak and Williamson, 1999), from guessed A* and Vr values for each U* cut point.

Full tables of these values with the corresponding A* and V_r are provided in Appendix B for Khalak and Williamson (Khalak and Williamson, 1999). Using these data and the U* values which were chosen for each dataset and constant for all iterations, a C_{lv} *expected* for converging at that A* and was also calculated and tabulated. This value essentially reproduces the values calculated as part of the improved convergence process used in section 4.4 for the Gharib data. This fact allows for the quality of convergences under the old and improved convergence criteria to be compared.

With these values in hand, it was possible to calculate the error (the difference between C_{lv} and C_{lv} expected) for each point. A mean error value of 0.1493 was calculuated in C_{lv} for the Khalak and Williamson (Khalak and Williamson, 1999) reproduction, which is within the acceptable range for C_{lv} variation used in proofing the system. Likewise, the standard deviation was calculated as 0.1834, again inside of the acceptable range during system proofing.

The new convergence criteria decided on for the Gharib dataset is that detailed in Chapter 3.5.7. That makes these figures very important, because the convergence criteria decided upon for improving the system and implemented per 3.5.7 for the Gharib (Gharib, 1999) reproduction was a $\Delta C_{lv} < 0.2$; this shows that although some individual points of the Khalak and Williamson data were outside of this improved convergence criterion, the mean and standard deviation of these data were within it.

4.4 Comparison with Gharib (1999).

Gharib's data (Gharib, 1999) were reproduced using the refined convergence criteria described in 5.3. They are based on a much higher m* value of m* = 28 instead the m* = 2.4 of Khalak and Williamson (Khalak and Williamson, 1999), but these experiments also used a low ζ value of $\zeta = 0.007$. Despite the fact

that m* > 20 is normally associated with experiments in air, these experiments were conducted in water by Gharib. One result of this difference in m*, however, is that the same hysterisis is not expected in these data, and indeed, only two branches were observed in both Gharib's free vibration experiments as well as in the simulations from the present study.

The higher m* value results in a fundamentally different response per Khalak and Williamson (Khalak and Williamson, 1999), who originally used their results reproduced in 4.3 to argue that the response amplitude was *primarily* dependent on m*. Gharib's dataset thus provides a very different response to simulate, using the same algorithm.

Gharib, unlike Khalak and Williamson varies u, velocity, in his free vibration response experiments. This provides an addition challenge for the simulation system, as in the simulation each set of runs is conducted at constant velocity in the forced motion to provide force coefficients for the simulation. Since Gharib's results have a different Re for each data point it is difficult to match Reynolds number. Instead, the simulation is run with constant Reynolds number close to the values in Gharib's experiments.

The results were found to be extremely good in matching the free vibration case from Gharib, and the same data format is followed below, with the amplitude response as a function of V_r shown in Fig.21.

These data are not *precisely* as good as the reproduction of Khalak and Williamson in matching the full range of data for V_r, with the range of the initial branch shifted toward lower V_r values. Generally, however, the same maximum values, positions of data-points, and range of values and trends remain comparable throughout both sets of data. Differences in Re did not appear to significantly affect the prediction method in this case. Fig.22 shows the plot of convergence

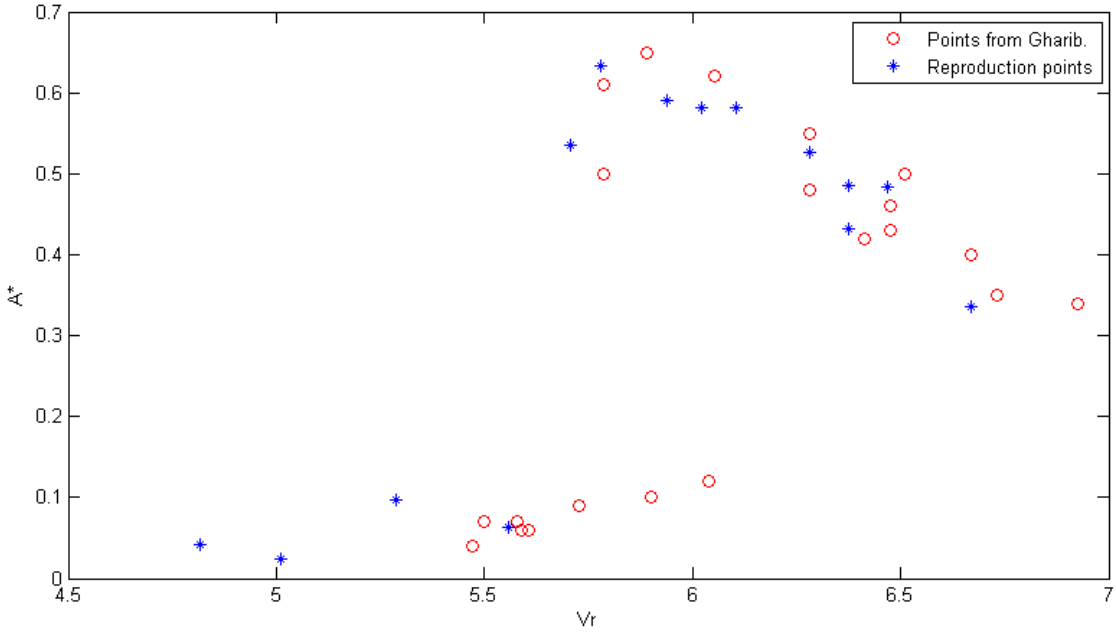

Figure 21: A* vs. V_r for the case of Gharib (Gharib, 1999) and the reproduction of Gharib's data using the forced motion simulation system.

paths overlaid with Gharib's data.

These data show the expected pattern over a more compressed range of convergence trajectories with little change in V_r across comparable V_r values to those for Khalak and Williamson (Khalak and Williamson, 1999) Fig.20, but without the switch to large changes in V_r toward higher V_r convergence points, likely because of the compressed range of these data. The results still show more noticeable changes in V_r in the area of lower V_r values for convergence, similar to Khalak and Williamson. Broadly this can be seen as a damped response for the convergence.

Finally, the same error calculations were made for the Gharib comparison as for the Khalak and Williamson case. It is important to note that of the 20 points compared, one of these points was converged upon using the old convergence criteria. The other 19 used the updated and improved convergence criteria. For the entire dataset, the result was a mean error of ΔC_{lv}= 0.1360, and a standard deviation of 0.1032, both significant improvements over the convergence criteria

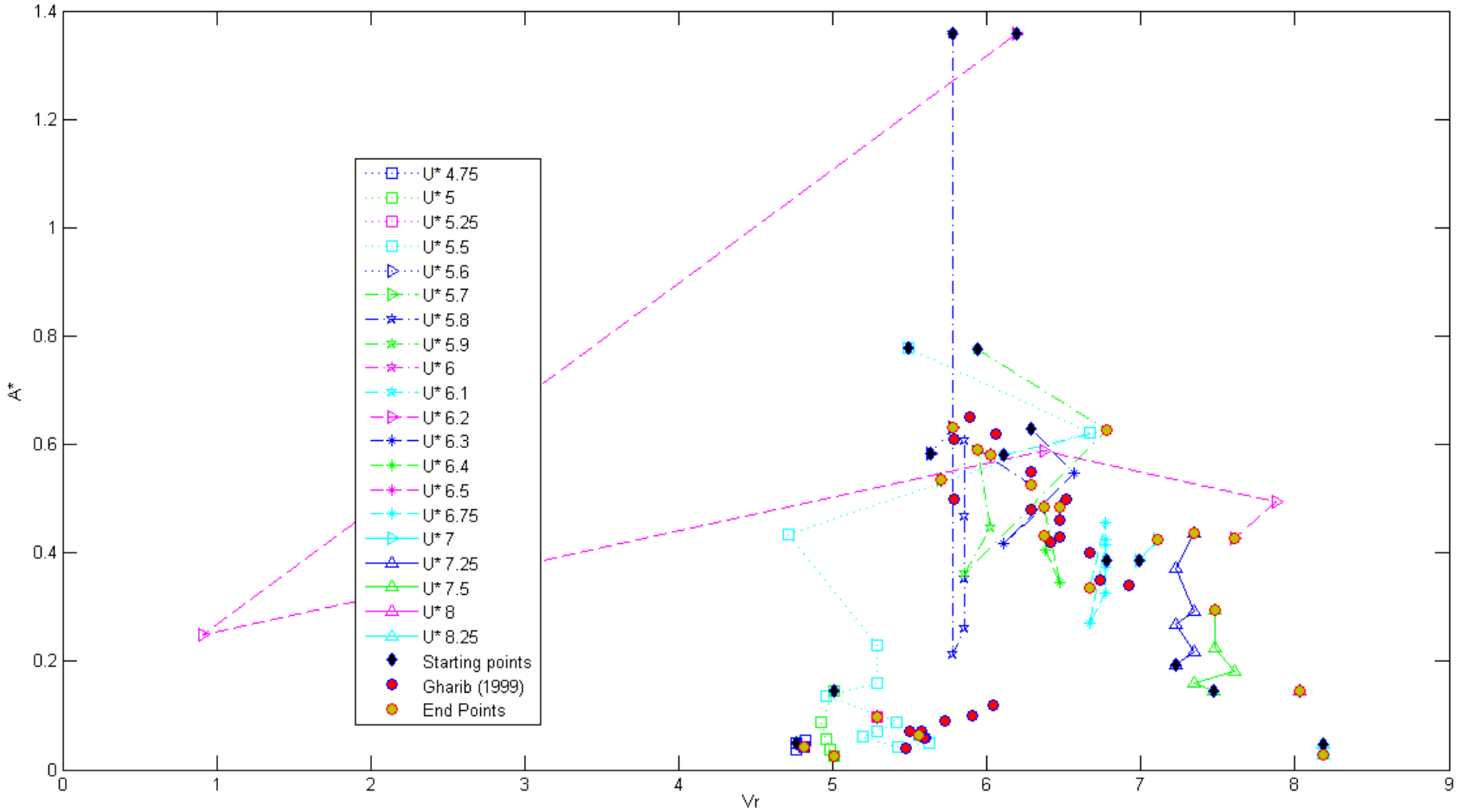

Figure 22: Plot of Convergence for Simulation of Gharib (Gharib, 1999)

used for Khalak and Williamson. With the single point excluded using the old convergence criteria, the remaining 19 points show a ΔC_{lv}= 0.1206 and a standard deviation of 0.0791. Based on these calculations and observations of these results it is likely that the convergence criteria could be successfully tightened in the future to ΔC_{lv}< 0.15 and C_{lv}> -0.05. The full tables of these data are available in Appendix C.

4.5 Observations

Based on these data as reported above, it is argued that the system results may be trusted for all cases involving vertical cylinders, regardless of m*, for low but varied ζ values, and for fixed or variable Reynolds number across a dataset. The cause of the system difficulties for horizontal cylinders and the possible relationship between the difficulties and that condition is unknown, though possibly due to the experimental setup, the way data is reported, and/or higher Re, and will be discussed more in Chapter 5.

Convergence improved between Khalak and Williamson (Khalak and Williamson, 1999) and Gharib (Gharib, 1999) due to the implementation of the convergence criteria described in 3.5.7. One of the main improvements in convergence ability between the two datasets is simply that for Gharib, negative values of C_{lv} were restricted to C_{lv}> -0.1 since convergence can never occur for negative C_{lv}values, so a convergence at a negative C_{lv} is a *true* error and should be much more strictly limited than at positive values where the multiple overlapping branches mean multiple convergences at a single value of V_r. However, since the mean error in C_{lv} reduces from 0.1493 to 0.1206, the improvement clearly goes much beyond simply solving the negative value problem.

Based on the improvement in mean error, as well as the elimination of convergence for outliers (ΔC_{lv}> 0.2), the Newton-Raphson method is observed to be

successful as implemented in this algorithm. Several U* values were repeatedly tested for convergence, with different initial amplitude guesses. In one case, the use of a higher A* than the expected value saw convergence after three iterations, and a lower A* saw convergence after seven iterations, but both correctly converged to values within the margin of error ($\Delta C_{lv} < 0.2$). A similar pattern was observed for many points at different U* values, where a variety of initial guesses ranging from A* = 0.2 to A* = 1.3 were tried over the course of the dataset for similar but different U* values. In these cases, the worst convergence performance was at low expected (and obtained) A* values, with the number of iterations being as high as 12 for cases of U* < 5.5, typically associated with low V_r and low A* values. In the case of high A* values the number of runs was more typically 3 - 5, but if the initial guess for A* was lower rather than higher than the value of convergence, the results tended toward 7 - 8 iterations to convergence. From literature (surveying the bibliography), this method has not been previously attempted to the knowledge of the author and represents a novel form of solving for convergence in VIV simulation.

Fig.23 shows the runs (iterations) to convergence for the reproduction of Khalak and Williamson (Khalak and Williamson, 1999), inclusive of multiple datapoints at the same value of U*. The mean number of runs to convergence was 5.7. Since the spatial area over which these iterations commenced varied (A* was not a constant guess, but could be very close to the expected outcome or very far, as could V_r, to intentionally test the system flexibility), this number is not generally applicable over the range of simulation data. Fig.23 illustrates that runs to convergence is not correlated with reduced velocity.

An interesting consequence of adopting the improved Newton-Raphson solver method for driving iterations is that the mean number of runs reduced, to only

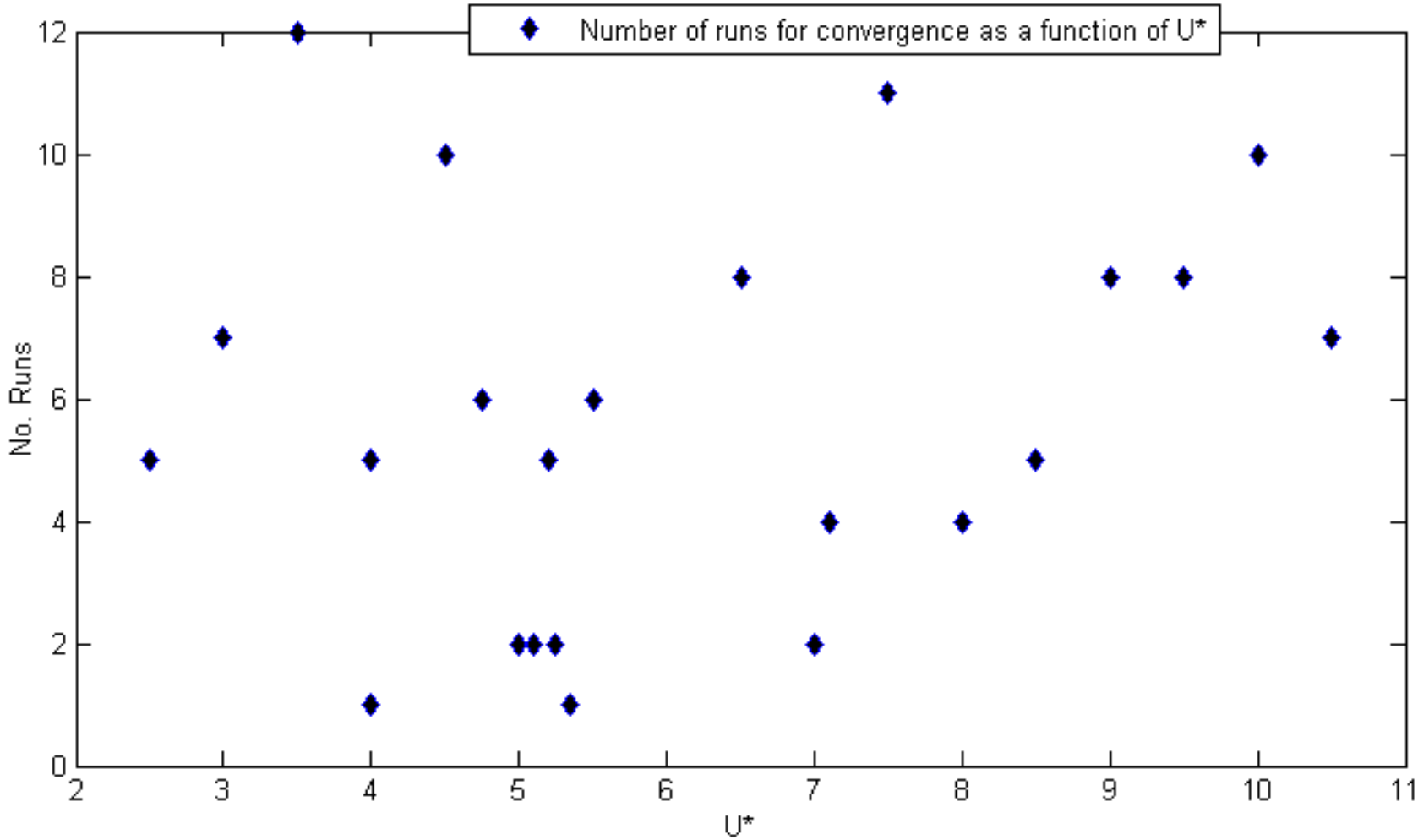

Figure 23: Iterations to Convergence for Khalak and Williamson (Khalak and Williamson, 1999) reproduction

3.9. However, this figure is of marginal value, though worth observing. These data for Gharib (Gharib, 1999) are provided in Fig.24.

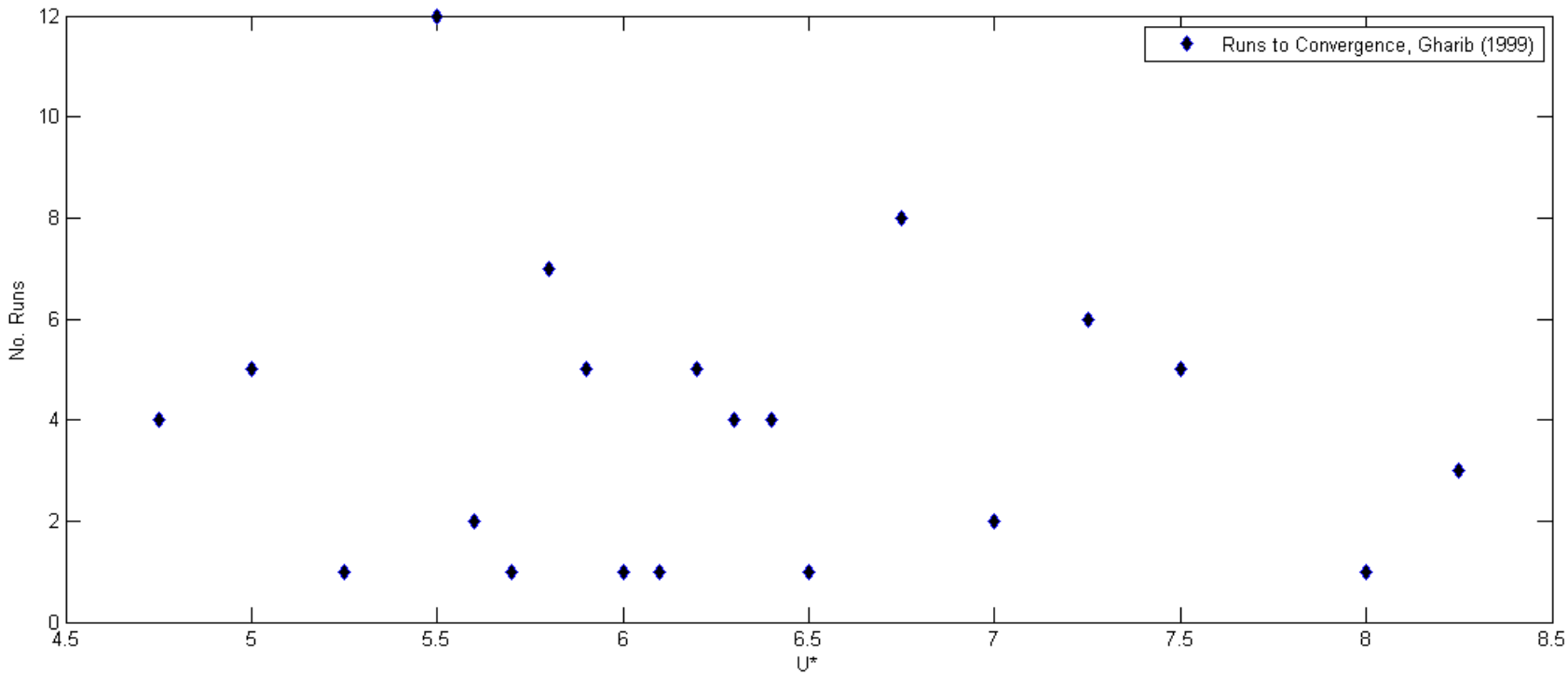

Figure 24: Iterations to Convergence for Gharib (Gharib, 1999) reproduction

CHAPTER 5

Conclusions and Recommendations

Problems caused by VIV are numerous and varied, presenting themselves throughout a wide range of engineering applications. Both problematic drilling risers for petroleum extraction and sustainable offshore wind towers experience VIV. Future extraction from manganese nodules conceivably shall also rely on systems of risers and slurry pipelines, for example.

These engineered systems require a level of precision in design which does not presently exist. Conservatism in design cannot work for ocean renewable energy to become competitive with traditional fossil fuels, while oil and gas exploration in deepwater cannot afford catastrophic failures under operation. To bring costs down, equipment and material must be precisely engineered and minimised. Doing this requires an ability to conduct detailed study on VIV as an important component of this process. This requires a truly adequate model of VIV, including 2-degree of freedom simulations which properly reflect the hydrodynamic forces observed in nature.

This work has been undertaken to acheive the kind of reduction in effort and complexity of research needed to improve VIV modeling in applications. The objective throughout this process has been to achieve a system which can provide on-demand simulation of VIV across a wide range of parameters. It has also been to make that system one which will ultimately see the same level of on-demand research applied to more accurate 2-degree of freedom and continuous system simulations which may be used to fine-tune fatigue design of immersed structures. The long term savings to be yielded from this improved understanding of VIV as a phenomenon and a hazard to immersed structures will only serve to

benefit and empower the development of offshore resources.

5.1 Principal Contributions of the Thesis

5.1.1 Development of the Algorithm.

The algorithm for semi-empirical simulation demonstrated in these results serves as the leading contribution. Unlike previous semi-empirical systems relying on massive pre-defined databases, this system will find a stable solution for simulating VIV, with significantly less experimental effort.

It also dispenses with the need to make inferences from data which may widely vary. A given cylinder with m* and ζ values which do not match precisely those of prior experimental data may not yield similar results, or those prior results may not be applicable to the particular case under study. With a very short outlay of time and no outlay of further resources, that specific unique cylinder may now be precisely simulated. Demonstration of the 1-degree of freedom case offers a simple expansion to unusual variations. Marginal changes in code would be required to the existing system to account for non-cylindrical structures or cylinders with damping devices. A mounting piece for a cylinder at an angle could easily be provided for the experimental rig and experiments run on such cases. Even with extremely wide differences between the test piece and the piece being simulated, the system has demonstrated reliable results and can be robustly used to simulate even very large cylinders as long as the Reynolds number constraints are met.

5.1.2 Simulation of 1-degree of freedom results.

Reliable reproduction of A*, U* points both as raw data and when normalized by f* into A*, V_r data have been demonstrated. These data reproduce curves from both Khalak and Williamson (Khalak and Williamson, 1999) and M. Gharib (Gharib, 1999), across order of magnitude differences in normalized mass (m*) values *and* damping ratio (ζ), resulting in a system that can operate across a

large range of the mass-damping parameter (m*ζ). A Reynolds number range of approximately 10,000 - 16,500 was also demonstrated across these experiments. Results included both fixed Reynolds number curves (Khalak and Williamson) and variable Reynolds number curves (Gharib) within the above range, including points from Gharib up to a Re = 25,000. The number of experimental runs for any single datapoint was consistently less than 18. This demonstrates that the system can reproduce 1-degree of freedom free vibration data at a substantial reduction in effort compared to the 70 experiment resolution for similar performance required in Morse and Williamson (Morse and Williamson, 2009).

5.1.3 On Demand Simulation

Validation of the system of on-demand VIV simulation has been demonstrated. With the success of the algorithm, the concept of using on-demand experiments directly combined and executed simultaneously with an iterative solver has been shown to be feasible. This outcome demonstrates the value of further development of the on-demand method for 2-degree of freedom and continuous system simulations.

5.1.4 Newton-Raphson Method

Likewise of interest is the successful use of the Newton Function itself. As observed in Chapter 3.5.7, this has not been previously demonstrated as a method for iterative solving in VIV simulation research. Therefore the method of solving for the model of body motion through iterations of the Newton Function, both simple and elegant, is completely new. It is an unexpected benefit of the project that it has been demonstrated by the improved convergence criteria implementation to work better than the traditional method of solving for the change in amplitude over time, and should be of interest and use in future experimental efforts.

5.2 Future Recommendations

5.2.1 Sparse Database

One future desire is that the prediction algorithm itself must be inherently capable of 'learning'; it should not repeat experiments that have been previously conducted, and should be able to obtain a solution simply from established data if required to converge on a solution for which it already has data. This functionality will be critical if developing this method for continuous systems with larger numbers of variables. Therefore, improvements to the data storage and implementation of an additional function which can do database search and retrieval is highly desirable.

5.2.2 2-degree of freedom implementation

This research entailed development of a general algorithm for combining on-demand experiments with the solution of the body equations of motion to predict VIV for the case of a rigid cylinder segment. Since the algorithm is general, increasing the degrees of freedom increases the number of parameters the solution must converge upon, yet needs only trivial programming changes in principle. The system has been necessarily designed to allow this expansion.

2-degree of freedom simulation will likely require an improved method for convergence and simulation. For example, in addition to the Newton Function, a Kriging analysis of the data from prior runs may be necessary to inform the selection of the next set of A^* and V_r parameters. Kriging would allow for the virtual geography of the XY plane in terms of its likelihood of containing the desired values for the stable solution versus those values already obtained through prior trials. This would allow for the area of the coordinates defining a possible region of convergence to be substantially reduced and allow the Newton Function iterator to focus on a narrow range for the final series of test runs which would

guarantee rapid convergence.

5.2.3 Testing of VIV suppression devices

In another opportunity, the existing system could easily accomodate any vertical cylinder with streamers, fairings, strakes or other VIV suppression devices. These fittings, normally used in reducing VIV oscillations on risers (Dahl, 2008), remain a subject of considerable design effort. On-demand VIV simulation could provide rapid and accurate comparison of an extremely large number of fittings with reproducable baselines. In doing so, more effective fittings could be isolated from a large range of design decisions. This would also potentially allow the development of broad rules or equations governing the design of the best fittings for a particular flow condition.

5.2.4 Continuous system simulations

As a further expansion on the 2-degree of freedom simulations that the algorithm's demonstration make possible to approach, full continuous system simulations could ultimately be implemented. This would require an overarching programme to implement combination of a series of runs representing different flow conditions at a series of discrete points along a riser. The system could on-demand call for additional experiments to refine the interaction of each section of the riser being separately simulated as 2-degree of freedom system until the entire riser is functioning iteratively as a continuous system.

5.2.5 Horizontal cylinder case

In principle, the use of a vertical or horizontal cylinder should not matter for the purposes of VIV research. There is no demonstrated phenomenon which would cause differences in the force coefficients between these cases. With all nondimensional parameters properly matched, one would only expect that the

vertical cylinder test rig could provide coefficients which would allow the simulation system to properly simulate these cylinders. That is not the case, however. In the specific situation of the Smogeli data (Smogeli et al., 2003), the use of a force-feedback mechanism to pseudosimulate free vibration VIV could cause error, but the Smogeli, et. al. data is in good agreement with several other VIV studies. This possibility does not exist for Vikestad (Vikestad et al., 1997) who had a genuine free vibration case. Therefore, uncertainty into the cause of this inability to reproduce data from Smogeli and Vikestad remain.

Experiments could be continued to see if any change in the system would allow it to simulate horizontal cylinders. Additional horizontal cylinder free vibration experiments could be located and reproduction of their results attempted to see if the trend continues or the results of Vikestad and Smogeli ultimately appear to be outliers. In the long run it could be possible that a proper understanding of some difference between horizontal and vertical cylinder alignments could be discovered, or else errors in the system corrected and the accuracy of the simulation system further improved.

LIST OF REFERENCES

Bearman, P. (1969). On vortex shedding from a circular cylinder in the critical reynolds number regime. *Journal of Fluid Mechanics*, 37:577–585.

Bearman, P. (1984). Vortex shedding from oscillating bluff bodies. *Annual Review of Fluid Mechanics*, 16:195–222.

Bearman, P. (2011). Circular cylinder wakes and vortex-induced vibrations. *Journal of Fluids and Structures*, 27:648–658.

Chaplin, J., Bearman, P., Cheng, Y., Fontaine, E., Graham, J., Herfjord, K., Huera-Huarte, F., Isherwood, M., Lambrakos, K., Larsen, C., Meneghini, J., Moe, G., Pattenden, R., Triantafyllou, M., and Willden, R. (2005). Blind prediction of laboratory measurements of vortex-induced vibrations of a tension riser. *Journal of Fluids and Structures*, 21:25–40.

Dahl, J. (2008). *Vortex-Induced Vibration of a Circular Cylinder with Combined In-line and Cross-flow Motion*. PhD thesis, Massachusetts Institute of Technology.

Gharib, M. (1999). *Vortex-Induced Vibration, Absence of Lock-in and Fluid Force Detection*. PhD thesis, California Institute of Technology.

Gopalkrishnan, R. (1993). *Vortex-Induced Forces on Oscillating Bluff Cylinders*. PhD thesis, Massachusetts Institute of Technology.

Govardhan, R. and Williamson, C. (2006). Defining the 'modified griffin plot' in vortex-induced vibration: Revealing the effect of reynolds number using controlled damping. *Journal of Fluid Mechanics*, 561:147–180.

Hover, FS. Techet, A. and Triantafyllou, M. (1998). Forces on oscillating uniform and tapered cylinders in crossflow. *Journal of Fluid Mechanics*, 363:97–114.

Jauvtis, N. and Williamson, C. (2004). The effect of two degrees of freedom on vortex-induced vibration at low mass and damping. *Journal of Fluid Mechanics*, 509:23–62.

Khalak, A. and Williamson, C. (1999). Motion, forces and mode transitions in vortex-induced vvibration at low mass damping. *Journal of Fluids and Structures*, 13:813–851.

Modarres-Sadeghi, Y., Mukundan, H., Dahl, J., Hover, F., and Triantafyllou, M. (2010). The effect of higher harmonic forces on fatigue life of marine risers. *Journal of Sound and Vibration*, 329:43–55.

Morse, T., Govardhan, R., and Williamson, C. (2008). The effect of end conditions on the vortex-induced vibration of cylinders. *Journal of Fluids and Structures*, 14:1227–1239.

Morse, T. and Williamson, C. (2008). The effect of reynolds number on the critical mass phenomenon in vortex-induced vibration. *Physics of Fluids*, 21.

Morse, T. and Williamson, C. (2009). Prediction of vortex induced vibration response by employing controlled motion. *Journal of Fluid Mechanics*, 634:5–39.

Mukundan, H., H. F. and Triantafyllou, M. (2010). A systematic approach to riser viv response reconstruction. *Journal of Fluids and Structures*, 26:722–746.

Norg, M. (2011). Untitled webforum post. [Online]. Available: http://forums.deltatau.com/printthread.php?tid=354.

Sarpkaya, T. (2004). A critical review of the intrinsic nature of vortex-induced vibrations. *Journal of Fluids and Structures*, 19:389–447.

Smogeli, O., Hover, F., and Triantafyllou, M. (2003). Force-feedback control in viv experiments. In *Proceedings of OMAE03*.

Vikestad, K., Vandiver, J., and Larsen, C. (1997). Experimental study of excited circular cylinder in current. In *Proceedings of OMAE97*.

Williamson, C. and Govardhan, R. (2004). Vortex-induced vibration. *Annual Review of Fluid Mechanics*, 36:413–55.

APPENDIX A

Force Coefficients and Charts used for Comparison

In this Appendix, the first table contains values of C_{lv} and C_m produced by single-iteration test runs of the experimental apparatus used in this thesis at a given A* and V_r that correspond with selected values from Morse and Williamson and Gopalkrishnan's forced motion experiments at the same A* and V_r.

actual A*	C_m	C_m	C_m	C_m	C_m
0.2	-0.486	-1.182	2.59	1.67	1.63
0.4	-0.686	-0.498	2.311	1.98	1.745
0.6	-0.55	-0.45	2.078	1.995	1.785
0.8	-1.05	-0.41	1.755	1.8614	1.7719
1	-1.29	-0.4	1.138	1.4029	1.6453
guess 1/Vr	0.1	0.149253731	0.2	0.25	0.303030303
actual 1/Vr	0.085	0.148	0.211	0.2529	0.2951

actual A*	C_lv	C_lv	C_lv	C_lv	C_lv
0.2	-0.085	0.233	-0.814	-0.193	-0.316
0.4	-0.16	0.0463	-0.791	-1.06	-1.5216
0.6	-0.37	-0.2	-0.752	-1.151	-2.5067
0.8	-0.52	-0.538	-0.356	-1.8827	-3.6275
1	-0.815	-1.08	-1.289	-3.0689	-3.7889
guess 1/Vr	0.1	0.149253731	0.2	0.25	0.303030303
actual 1/Vr	0.085	0.148	0.211	0.2529	0.2951

Table A.1: System Proofing C_{lv}/C_m result data used in reference points obtained from graphs reproduced below and shown in figure A.2.

actual A*	C_m	C_m	C_m	C_m	C_m
0.2	-0.65	-0.7	2.5	1.45	1.4
0.4	-0.58	-0.42	2.35	1.5	1.4
0.6	-0.55	-0.42	1.95	1.65	1.5
0.8	-0.59	-0.45	1.65	1.75	1.55
1	-0.55	-0.49	1.6	1.5	1.45
actual 1/Vr	0.085	0.148	0.211	0.2529	0.2951

actual A*	C_lv	C_lv	C_lv	C_lv	C_lv
0.2	-0.075	0.2	-0.75	-0.175	-0.25
0.4	-0.11	0.14	-1.1	-1.1	-1.3
0.6	-0.3	-0.09	-0.1.1	-1.1	-2.5
0.8	-0.45	-0.42	-0.3	-2.0	-2.7
1	-0.6	-0.9	-1.05	-3.0	-3.5
actual 1/Vr	0.085	0.148	0.211	0.2529	0.2951

Table A.2: System Proofing C_{lv}/C_m comparison data acquired from figures below.

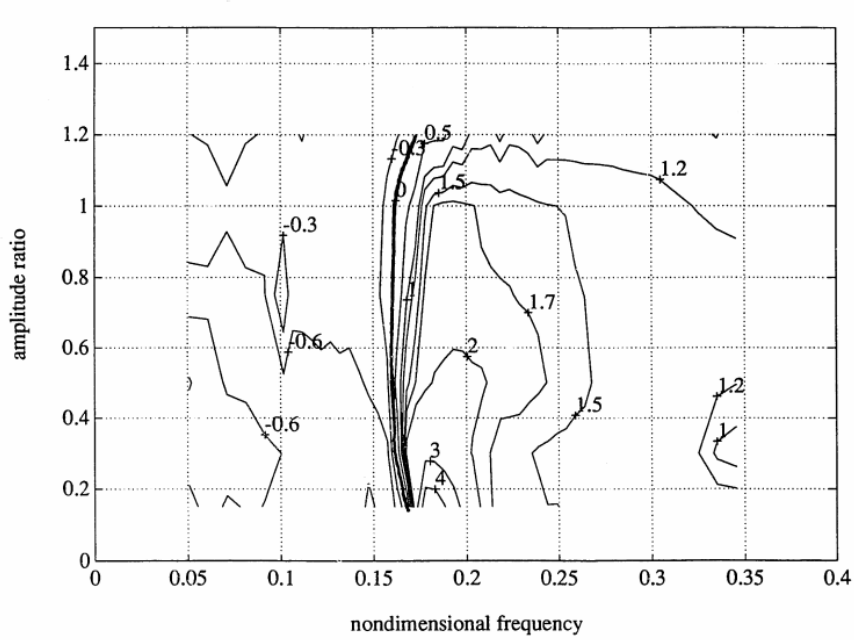

Figure 3-16: Contours of the added mass coefficient; sinusoidal oscillations.

80

Figure A.1: C_m from Gopalkrishnan for forced motion proofing reference.

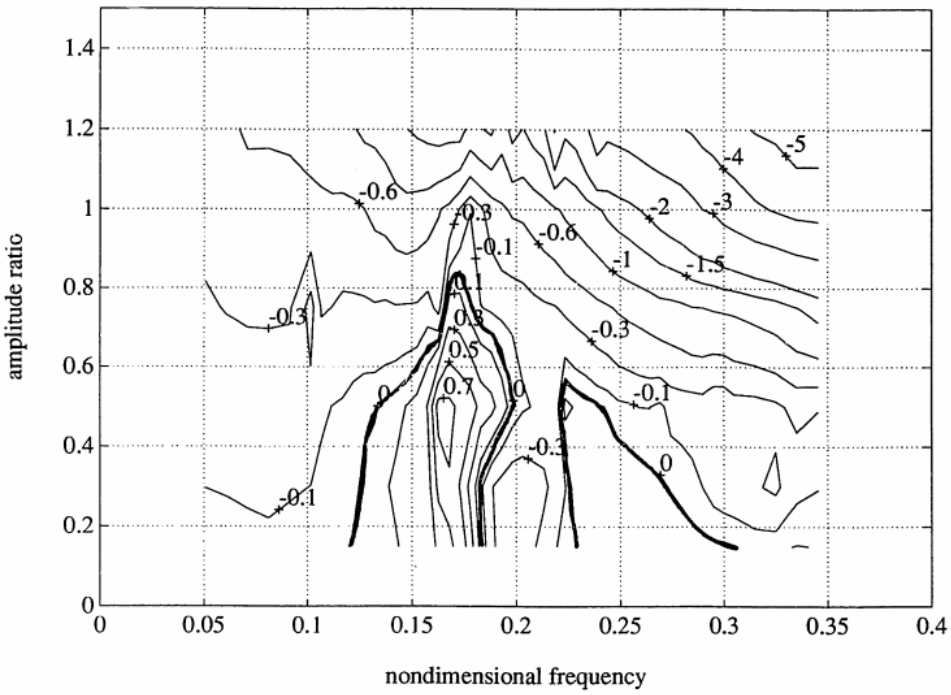

Figure 3-14: Contours of the lift coefficient in phase with velocity; sinusoidal oscillations.

Figure A.2: C_{lv} from Gopalkrishnan for forced motion proofing reference.

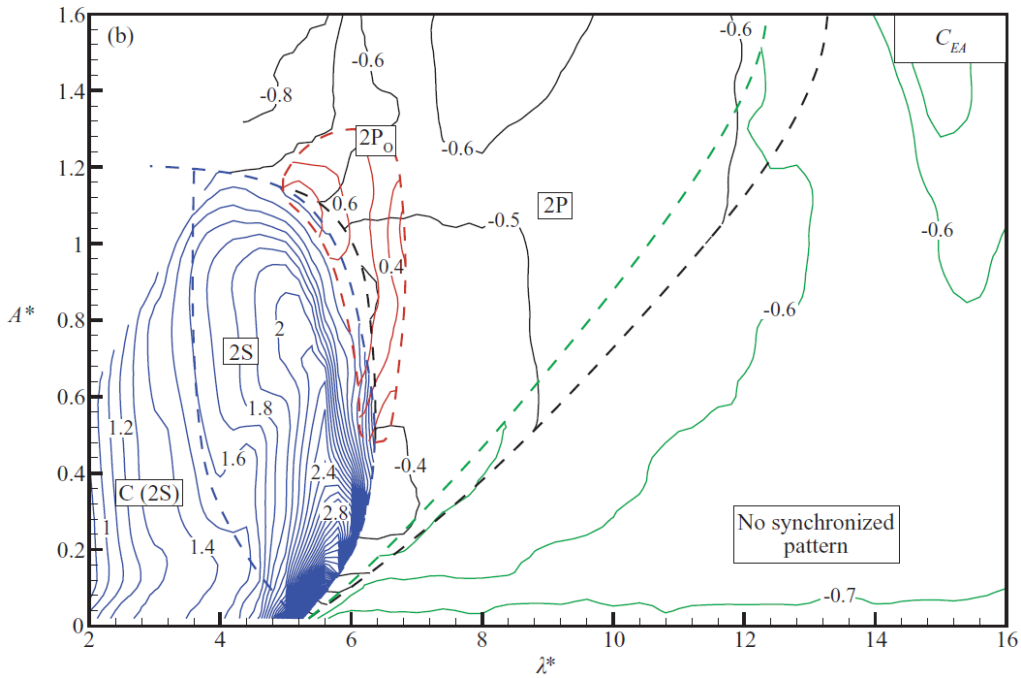

Figure A.3: C_m from Morse and Williamson (2009) for forced motion proofing reference.

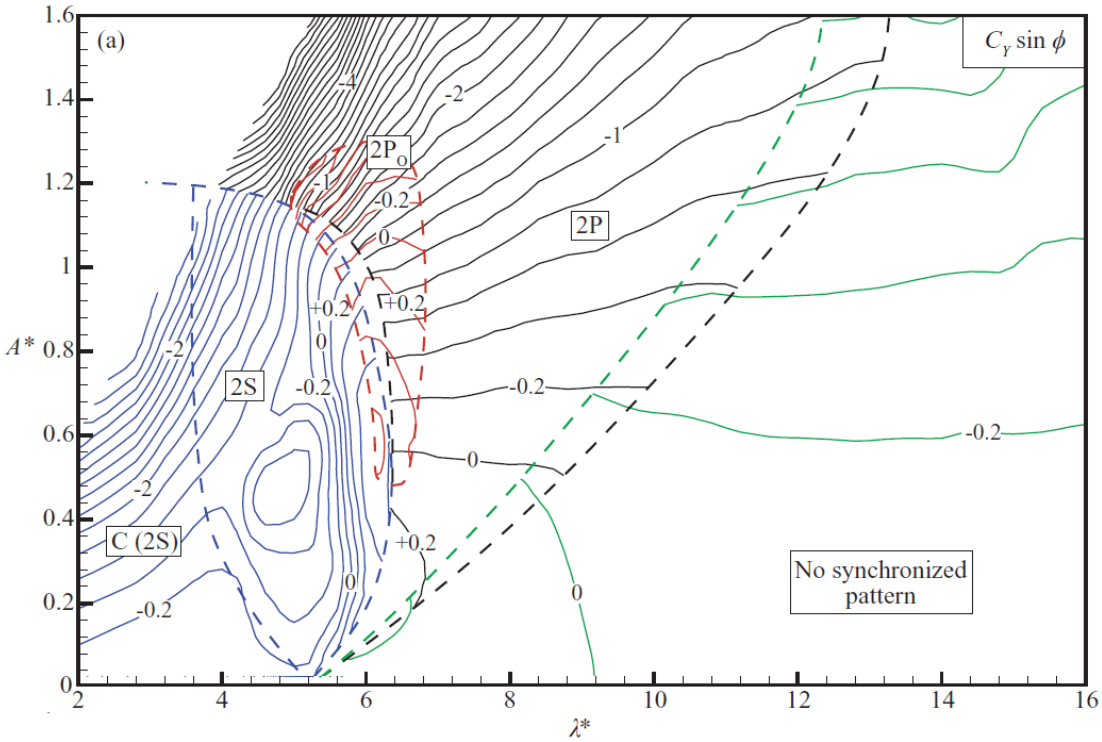

Figure A.4: C_{lv} from Morse and Williamson (2009) referenced for forced motion proofing.

APPENDIX B

Tabular Clv Data, Khalak and Williamson (1999)

Vr	A*	Clv	Clv expected	Difference
6.4511	0.54088	-0.17344	0.053753	0.22719
6.9505	0.60266	0.054416	0.051619	0.0027973
7.3718	0.49898	0.050071	0.03761	0.012461
7.8539	0.48572	-0.0051598	0.032215	0.037375
9.0279	0.0042822	0.036262	0.00049416	0.035768
4.4063	0.16992	-0.2096	0.035712	0.24531
4.4055	0.52234	-0.029989	0.10402	0.13401
4.982	0.73933	0.10052	0.12369	0.023167
4.9484	0.78823	0.16508	0.13016	0.034928
5.0873	0.42294	-0.32771	0.066626	0.39434
5.7342	0.76207	0.055564	0.1007	0.045133
5.1228	0.78513	0.2916	0.12165	0.16995
5.0174	0.87658	0.2566	0.13608	0.12051
8.4102	0.4408	-0.76531	0.025696	0.79101
8.8142	0.2783	0.12752	0.014619	0.1129
9.2735	0.22836	-0.14132	0.010802	0.15212
9.5161	0.11627	0.20197	0.0050916	0.19688
10.04	0.083169	-0.21551	0.0032877	0.2188
3.504	0.19557	0.065681	0.066452	0.00077045
4.0105	0.19534	0.080574	0.050744	0.02983

Table B.1: Tabular C_{lv} and C_{lv} expected data for Khalak and Williamson, using change in A* convergence criteria.

APPENDIX C

Tabular Clv Data, Gharib (1999)

Vr	A*	C_{lv}	C_{lv} expected	Difference
4.8154	0.041384	-0.041851	0.043981	0.085832
5.0108	0.024237	-0.40484	0.023516	0.42836
5.5564	0.0633	0.16727	0.050351	0.11692
5.7793	0.63255	0.31749	0.47512	0.15762
5.7052	0.53461	0.39536	0.39962	0.0042598
6.2826	0.52667	0.34553	0.35135	0.005821
5.9379	0.5899	0.21417	0.40932	0.19515
5.2865	0.097073	-0.027366	0.085023	0.11239
6.0226	0.5818	0.21853	0.39139	0.17286
6.1065	0.58182	0.12682	0.37969	0.25287
7.6048	0.42664	0.10252	0.21996	0.11744
6.3749	0.48569	0.23927	0.29397	0.054706
6.3752	0.43155	0.31915	0.25711	0.06204
6.4689	0.48355	0.05455	0.27955	0.225
6.6688	0.33551	0.033722	0.18118	0.14746
7.1049	0.42456	0.060907	0.20751	0.14661
7.4784	0.29453	-0.072059	0.12765	0.19971
7.347	0.43602	-0.0097296	0.19899	0.20872
8.0299	0.14455	0.052651	0.0547	0.0020486
8.1794	0.026654	0.034324	0.0096019	0.024722

Table C.1: Tabular C_{lv} and C_{lv} expected data for Gharib (1999) using Newton-Raphson Method except for Row 2

APPENDIX D

Derivations of the Nondimensional amplitude and frequency defining the 1-degree of freedom VIV case

D.1 Explanation of the Derivation

This part of the appendix contains a series of derivations related to the basic equations of body motion for the 1-degree of freedom spring-mass-damper case of VIV. The derivation makes usual assumptions of an inviscid and incompressible fluid and a 2-dimensional flow case. It serves to reduce the dimensionalized case of the equations of body motion based on the 1-degree of freedom spring mass damper into the nondimensional coefficients that are used to define the motion for this simulation and the related forced motion experiments, the final resolved A* and f* used throughout the thesis that originate with the basic spring-mass-damper system.

D.2 Variable Definitions

Contained in the table "Derivation Variable Definitions" are the descriptions of the variables used within these derivations. Contained in the table "Nondimensional Coefficients in the Derivation" are descriptions of the nondimensional coefficients solved for or that components of the equations in the derivations are reduced to over the course of working them.

Variable	Definition
m	mass
b	coefficient of damping
k	spring constant
y	transverse (normal to flow) position
f	frequency
F	force
ω	angular velocity
ϕ	phase angle
m_a	equivalent mass from forcing term
b_a	equivalent damping from forcing term
D	Diameter of Cylinder
L	Length of Cylinder
U	Characteristic directional flow speed
D	Diameter of Cylinder
ρ	Density of water
f_n	System natural frequency.

Table D.1: Derivation Variable Definitions

Nondimensional Coefficient	Definition
A*	Nondimensional Amplitude
f*	Frequency ratio (nondimensional frequency)
ζ	Damping ratio
U*	Nominal Reduced Velocity / Nondimensional velocity
C_L	Coefficient of Lift
C_M	Coefficient of Added Mass
m*	Mass ratio (nondimensional mass)

Table D.2: Nondimensional Coefficients in the Derivation

D.3 Derivation

D.3.1 Initial Derivation of m_a and b_a

The first component of the derivation is for m_a and b_a, the effective added mass and the effective added damping. These terms are based on the principle of rewriting the basic equation of motion my"+by'+ky=F in terms which eliminate the existing of the forcing function by creating an equivalent mass and equivalent

damping which represent the applied force to the body. This makes the iterative solution of the problem undertaken in this thesis possible from a mathematical perspective by permitting the nondimensionalisation of the problem, when the co-dependence of m_a and b_a necessitate it in the first place.

$$my'' + by' + ky = F$$

$$y(t) = y_o \cos(2\pi f t)$$

$$y'(t) = -y_o 2\pi f \sin(2\pi f t)$$

$$y''(t) = -y_o 4\pi^2 f^2 \cos(2\pi f t)$$

The first component comprises the decomposition of the forcing term in relation to the first, second and third derivatives of the position of the cylinder undgoing VIV. It establishes the component relationships required for the derivation of m_a,b_a.

$$my'' + by' + ky = F$$

$$F(t) = F_o \sin(\omega t + \phi) \Rightarrow$$

$$F = F_o \cos(\omega t + \phi)$$

$$= F_o \cos\phi \cos(\omega t) - F_o \sin\phi \sin(\omega t) \Rightarrow$$

$$my'' + by' + ky = F_o \cos\phi \cos(\omega t) - F_o \sin\phi \sin(\omega t) \Rightarrow$$

$$my'' + by' + ky = m_a y'' - b_a y' \Rightarrow$$

$$(m + m_a)y" + (b + b_a)y' + ky = 0$$

The second component decomposes the forcing term into m_a, b_a, accounting for the different phase angles of the acceleration and velocity dependent force terms.

The nature of these phase angles results from the derivatives of position into velocity and acceleration as demonstrated above.

D.3.2 Derivation for A*

This is the component of the derivation for A*. Since A* and f* are dependent upon each other, the derivation is not resolvable independently of f*, however, it is presented separately for convenient since the problem involves characterising the equation by simultaneous solution for both A* and f*.

$$my'' + by' + ky = F_o \cos(\omega t + \phi)$$
$$\frac{my''}{0.5\rho U^2 DL} + \frac{by'}{0.5\rho U^2 DL} + \frac{ky}{0.5\rho U^2 DL} = \frac{F_o \cos(\omega t + \phi)}{0.5\rho U^2 DL}$$
$$C_L = \frac{F_o}{0.5\rho U^2 DL}$$
$$\frac{my''}{0.5\rho U^2 DL} + \frac{by'}{0.5\rho U^2 DL} + \frac{ky}{0.5\rho U^2 DL} = C_L \cos(\omega t + \phi)$$

With C_L now incorporated, giving us the basic coefficient of lift, establishment of the full equation can begin, starting by listing additional components required.

$$\text{For } f_n = \frac{\sqrt{\frac{k}{m}}}{2\pi}, U* = \frac{2U\pi}{\sqrt{\frac{k}{m}}D}$$

$$\text{And, } b = 4\pi\zeta m f_n;\ k = 4\pi^2 f_n m$$

$$\frac{my''}{0.5\rho U^2 DL} + \frac{4\pi\zeta m f_n y'}{0.5\rho U^2 DL} + \frac{4\pi^2 f_n m y}{0.5\rho U^2 DL} = C_L \cos(2\pi f t + \phi)$$
$$0.5\rho U^2 L C_L \cos(2\pi f t + \phi) = \frac{F_o 4\pi^2 f^2 m \cos(\omega t)}{D} - \frac{F_o m\omega^2 \cos(\omega t)}{D} - \frac{F_o 4\omega\pi\zeta m f_n \sin(\omega t)}{D} \Rightarrow$$
$$\frac{F_o}{D} = \frac{0.5 C_L \rho U^2 L \cos(\phi) cos(\omega t) - 0.5 C_L \rho U^2 L \sin(\phi)\sin(\omega t)}{(4\pi^2 f_n^2 m - m\omega^2)\cos(\omega t) - 4\pi\zeta m f_n \sin(\omega t)\omega}$$

Whereas for $F = F_o$, $\cos \to 0$;

Finally, having defined F_o, and incorporating additional definitions of U* and f* based on equivalencies to the first set of definitions, we may now fully write the equation for A* in nondimensional form.

$$\frac{F_o}{D} = \frac{0.5C_L\rho U^2 L\sin(\phi)\sin(\omega t)}{4\pi\zeta m f_n \sin(\omega t)\omega}$$

$$\frac{F_o}{D} = \frac{0.5C_L\rho U^2 L\sin(\phi)}{4\pi\zeta m f_n \omega}$$

Then, as m* is defined as $m* = \frac{4m}{\pi\rho D^2 L}$,

$$\frac{F_o}{D} = \frac{C_L U^2 \sin(\phi)}{2\pi^2\zeta m * f_n D^2\omega}$$

Defining $U* = \frac{u}{f_n D}$; $f* = \frac{f}{f_n}$,

$$\frac{F_o}{D} = \frac{C_L \sin(\phi) U *^2 f}{2\pi^2 m * \zeta f * \omega}\frac{2\pi}{2\pi} \Longrightarrow$$

$$\frac{F_o}{D} = \frac{C_L \sin(\phi) U*^2}{4\pi^3 m * f * \zeta} = A*$$

D.3.3 Derivation for f*

And for f*, the problem is rearranged and solved in nondimensional terms of f*, again based on the co-dependency of f* and A* that is fundamental to the iterative process reflected in this problem (and based on the fact that both m_a and b_a are codependent upon each other).

$$\frac{F_o}{D}(4\pi^2 f_n^2 m - 4m\pi^2 f^2) = C_L \rho U^2 L \cos(\phi) \Rightarrow$$

$$f_n^2 - f^2 = \frac{0.5 C_L \cos(\phi)\rho U^2 L}{4A * \pi^2 m} \Rightarrow$$

$$1 - \frac{f^2}{f_n} = \frac{0.5 C_L \cos(\phi)\rho U^2 L}{4A * \pi^2 m f_n}$$

$$\text{As } C_m = \tfrac{1}{2\pi^3}\tfrac{C_L \cos(\phi)}{A*}(\tfrac{U*}{f*})^2,$$

$$\frac{-f^2}{f_n^2} = \frac{\pi}{4} C_m (\frac{\rho L D^2}{m}) - 1 \Rightarrow$$

$$\frac{-f^2}{f_n^2} = C_m (\frac{1}{m*}) - 1 \Rightarrow$$

$$\frac{f}{f_n} = \sqrt{1 - \frac{C_m}{m*}} \Rightarrow$$

$$f* = \sqrt{1 - \frac{C_m}{m*}}$$

Thus the co-dependent nature of A* and f* requiring the iterative solution is demonstrated, and the final useful arrangement of A* and f* shown.

BIBLIOGRAPHY

Bearman, P. (1969). On vortex shedding from a circular cylinder in the critical reynolds number regime. *Journal of Fluid Mechanics*, 37:577–585.

Bearman, P. (1984). Vortex shedding from oscillating bluff bodies. *Annual Review of Fluid Mechanics*, 16:195–222.

Bearman, P. (2011). Circular cylinder wakes and vortex-induced vibrations. *Journal of Fluids and Structures*, 27:648–658.

Chaplin, J., Bearman, P., Cheng, Y., Fontaine, E., Graham, J., Herfjord, K., Huera-Huarte, F., Isherwood, M., Lambrakos, K., Larsen, C., Meneghini, J., Moe, G., Pattenden, R., Triantafyllou, M., and Willden, R. (2005). Blind prediction of laboratory measurements of vortex-induced vibrations of a tension riser. *Journal of Fluids and Structures*, 21:25–40.

Dahl, J. (2008). *Vortex-Induced Vibration of a Circular Cylinder with Combined In-line and Cross-flow Motion*. PhD thesis, Massachusetts Institute of Technology.

Gharib, M. (1999). *Vortex-Induced Vibration, Absence of Lock-in and Fluid Force Detection*. PhD thesis, California Institute of Technology.

Gopalkrishnan, R. (1993). *Vortex-Induced Forces on Oscillating Bluff Cylinders*. PhD thesis, Massachusetts Institute of Technology.

Govardhan, R. and Williamson, C. (2006). Defining the 'modified griffin plot' in vortex-induced vibration: Revealing the effect of reynolds number using controlled damping. *Journal of Fluid Mechanics*, 561:147–180.

Hover, FS. Techet, A. and Triantafyllou, M. (1998). Forces on oscillating uniform and tapered cylinders in crossflow. *Journal of Fluid Mechanics*, 363:97–114.

Jauvtis, N. and Williamson, C. (2004). The effect of two degrees of freedom on vortex-induced vibration at low mass and damping. *Journal of Fluid Mechanics*, 509:23–62.

Khalak, A. and Williamson, C. (1999). Motion, forces and mode transitions in vortex-induced vvibration at low mass damping. *Journal of Fluids and Structures*, 13:813–851.

Modarres-Sadeghi, Y., Mukundan, H., Dahl, J., Hover, F., and Triantafyllou, M. (2010). The effect of higher harmonic forces on fatigue life of marine risers. *Journal of Sound and Vibration*, 329:43–55.

Morse, T., Govardhan, R., and Williamson, C. (2008). The effect of end conditions on the vortex-induced vibration of cylinders. *Journal of Fluids and Structures*, 14:1227–1239.

Morse, T. and Williamson, C. (2008). The effect of reynolds number on the critical mass phenomenon in vortex-induced vibration. *Physics of Fluids*, 21.

Morse, T. and Williamson, C. (2009). Prediction of vortex induced vibration response by employing controlled motion. *Journal of Fluid Mechanics*, 634:5–39.

Mukundan, H., H. F. and Triantafyllou, M. (2010). A systematic approach to riser viv response reconstruction. *Journal of Fluids and Structures*, 26:722–746.

Norg, M. (2011). Untitled webforum post. [Online]. Available: http://forums.deltatau.com/printthread.php?tid=354.

Sarpkaya, T. (2004). A critical review of the intrinsic nature of vortex-induced vibrations. *Journal of Fluids and Structures*, 19:389–447.

Smogeli, O., Hover, F., and Triantafyllou, M. (2003). Force-feedback control in viv experiments. In *Proceedings of OMAE03*.

Vikestad, K., Vandiver, J., and Larsen, C. (1997). Experimental study of excited circular cylinder in current. In *Proceedings of OMAE97*.

Williamson, C. and Govardhan, R. (2004). Vortex-induced vibration. *Annual Review of Fluid Mechanics*, 36:413–55.